Fluid-structure interaction for shear-dependent non-Newtonian fluids

A. Hundertmark-Zaušková*, M. Lukáčová-Medviďová*†, G. Rusnáková*‡

Contents

*Institute of Mathematics, Johannes Gutenberg University, Staudingerweg 9, 55099 Mainz, Germany
†corresponding author: lukacova@uni-mainz.de
‡Institute of Mathematics, Pavol Jozef Šafárik University, Jesenná 5, 040 01 Košice, Slovakia

Abstract

We present our recent results on mathematical modelling and numerical simulation of non-Newtonian flows in compliant two-dimensional domains having applications in hemodynamics. Two models of the shear-thinning non-Newtonian fluids, the power law Carreau model and the logarithmic Yeleswarapu model, will be considered. For the structural model the generalized string equation for radially symmetric tubes will be generalized to stenosed vessels and vessel bifurcations.

The arbitrary Lagrangian-Eulerian approach is used in order to take into account moving computational domains. To represent the fluid-structure interaction we use two different methods: the global iterative approach and the kinematical splitting. We will show that the latter method is more efficient and stable without any additional subiterations. The analytical result for the existence of a weak solution for the shear-thickening power-law fluid is based on the global iteration with respect to the domain deformation, energy estimates, compactness arguments using the semi-continuity in time and the theory of monotone operators. The numerical part of paper contains several experiments for the Carreau and the Yeleswarapu model, comparisons of the non-Newtonian and Newtonian models and the results for hemodynamical wall parameters; the wall shear stress and the oscillatory shear index. Numerical experiments confirm higher order accuracy and the reliability of new fluid-structure interaction methods.

keywords: non-Newtonian fluids, fluid-structure interaction, shear-thinning flow, hemodynamical wall parameters, stenosis, kinematical splitting, numerical stability, weak solution

1 Introduction

In the recent years there is a growing interest in the use of mathematical models and numerical methods arising from other fields of computational fluid dynamics in hemodynamics, see, e.g., [6, 8, 18, 19, 21, 27, 31, 36, 37, 39, 41, 40] just to mention some of them.

Many numerical methods used for blood flow simulations are based on the Newtonian model using the Navier-Stokes equations. This is efficient and useful, especially if the flow in large arteries is modeled. However, in small vessels or dealing with patients with a cardiovascular disease more complex models for blood rheology should be considered [31]. In capillaries blood is even not a homogenized continuum and more precise models, for example mixture theories need to be used. But even in the intermediate-size vessels the non-Newtonian behavior of blood has been demonstrated, see, e.g., [2], [43] and the references therein. In fact, blood is a complex mixture showing several non-Newtonian properties, such as the shear-thinning, viscoelasticity [48], [49] the yield stress or the stress relaxation [43].

The aim of this overview paper is to report on our recent results on mathematical and numerical modelling of shear-dependent flow in moving vessels. The application to hemodynamics will be pointed out. We will address the significance of non-Newtonian models for reliable hemodynamical modelling. In particular, we will show that the rheological properties of fluid have an influence on the wall deformation as well as on the

hemodynamical wall parameters, such as the wall shear stress and oscillatory shear index. Consequently these models yield a more reliable prediction of critical vessel areas, see also our previous results [28, 29, 24].

The paper is organized as follows. In Section 2 we recall the conservation laws for shear-dependent fluids and present typical models for non-constant blood viscosity. The generalized string model for the vessel deformation [40] is generalized to the case of reference radius, which is dependent on longitudinal variable. The derivation of this model for radially symmetric domains follows in Section 3.

Section 4 is devoted to two strategies to model the coupling between a fluid and a structure. *The global iterative method* with respect to the domain, presented in Section 4.1, provides besides the numerical scheme also a strategy to prove the existence of a weak solution. Mathematical analysis of the well-posedness of a coupled fluid-structure model arising from the blood flow in a compliant vessel is of great interest. In the literature there are already several results for the Newtonian fluid flow in time-dependent domains, see, e.g., [4, 5, 7, 6, 9, 10, 11, 12, 13, 20, 22, 23, 33, 47, 51] and others. The well-posedness of non-Newtonian fluids has been studied only in the fixed domains, see, e.g., [17, 34, 35, 50]. In these works the technique of monotone operators and the Lipschitz- or L^∞-truncation techniques are applied in order to control the additional nonlinearities in the diffusion terms arising from the non-Newtonian viscosity. In this overview paper we also present our recent result on the existence of a weak solution for the shear-thickenning fluid in compliant vessels, cf. [25]. The proof is based on the global iterative method with respect to the domain deformation [13, 51], theory of monotone operators as well as the techniques for moving domains developed in [7, Chambolle, Desjarden, Esteban, Grandmont].

The second fluid-structure interaction approach, that will be presented in Section 4.2, is the loosely-coupled fluid-structure interaction algorithm based on the *kinematical splitting* [21]. This is a novel way how to avoid instabilities due to the added mass effect and the additional stabilization through subiterations. Subsection 4.2.1 is devoted to stability analysis of the kinematical splitting method. Further details can be found in our recent paper [28].

Results of numerical experiments are described in Section 5. We apply both fluid-structure interaction methods and compare domain deformations as well the hemodynamical wall indices measuring the danger of atherosclerotic plaque caused by temporal oscillation or low values of the wall shear stress. We use two types of data: the model data proposed by Sequeira and Nadau [31] and the physiological data from the iliac artery and the carotid bifurcation measurements. In the hemodynamical wall parameters the effects due to the fluid-structure interaction as well as the blood rheology have been observed. Finally the experimental order of convergence for a rigid as well as a moving domain for both fluid-structure interaction methods will be investigated. In the case of kinematical splitting method second order convergence will be confirmed.

2 Mathematical model for shear-dependent fluids

Flow of incompressible fluid is governed by the momentum and the continuity equation

$$\begin{aligned} \rho\frac{\partial \boldsymbol{u}}{\partial t} + \rho\left(\boldsymbol{u}\cdot\nabla\right)\boldsymbol{u} - \operatorname{div}\left[2\mu\mathbf{D}(\boldsymbol{u})\right] + \nabla p &= \boldsymbol{f} \\ \operatorname{div}\boldsymbol{u} &= 0. \end{aligned} \tag{1}$$

Here ρ denotes the constant density of fluid, $\boldsymbol{u} = (u_1, u_2)$ the velocity vector, p the pressure, $\mathbf{D}(\boldsymbol{u}) = \frac{1}{2}(\nabla\boldsymbol{u} + \nabla\boldsymbol{u}^T)$ the deformation tensor and μ the viscosity of the fluid. In the literature various non-Newtonian models for the blood flow can be found. Here we will consider shear-dependent fluids, in particular the Carreau model and the Yeleswarapu-viscosity model [48], see also Fig. 1. For the Carreau model the viscosity function depends on the shear rate $|\mathbf{D}(\boldsymbol{u})| = \sqrt{\mathbf{D}:\mathbf{D}} = \sqrt{tr(\mathbf{D}^2)}$ in the following way

$$\mu = \mu(\mathbf{D}(\boldsymbol{u})) = \mu_\infty + (\mu_0 - \mu_\infty)(1 + |\gamma\mathbf{D}(\boldsymbol{u})|^2)^q, \quad q = \frac{p-2}{2} \leq 0, \tag{2}$$

where $q, \mu_0, \mu_\infty, \gamma$ are rheological parameters. According to [48] the physiological values for blood are $\mu_0 = 0.56P$, $\mu_\infty = 0.0345P$, $\gamma = 3.313$, $q = -0.322$. Note that in the case $q = 0$ the model reduces to the linear Newtonian model used in the Navier-Stokes equations. The Yeleswarapu viscosity model reads

$$\mu = \mu(\mathbf{D}(\boldsymbol{u})) = \mu_\infty + (\mu_0 - \mu_\infty)\frac{\ln(1+\gamma|\mathbf{D}(\boldsymbol{u})|) + 1}{(1+\gamma|\mathbf{D}(\boldsymbol{u})|)}. \tag{3}$$

The physiological measurements give $\mu_0 = 0.736P$, $\mu_\infty = 0.05P$, $\gamma = 14.81$ [48]. Time-dependent computational domain

$$\Omega(\eta(t)) \equiv \left\{(x_1, x_2) :\ -L < x_1 < L,\ 0 < x_2 < R_0(x_1) + \eta(x_1, t)\right\},\ 0 \leq t \leq T$$

is given by a reference radius function $R_0(x_1)$ and an unknown free boundary function $\eta(x_1, t)$ describing the domain deformation. For simplicity we will also use a shorter notation $\Omega_t := \Omega(\eta(t))$. We restrict ourselves to two-dimensional domains.
In order to capture movement of a deformable computational domain and preserve the rigidness of inflow and outflow parts, the conservation laws are rewritten using the so-called ALE (**Arbitrary Lagrangian-Eulerian**) mapping $\mathcal{A}_t$, see Fig. 3. It is a continuous bijective mapping from the reference configuration Ω_{ref}, e.g. at time $t = 0$, onto the current one $\Omega_t = \Omega(\eta(t))$, $\mathcal{A}_t : \Omega_{ref} \to \Omega_t$.
Introducing the so-called ALE-derivative

$$\frac{\mathcal{D}^{\mathcal{A}}\boldsymbol{u}(\boldsymbol{x},t)}{\mathcal{D}t} := \left.\frac{\partial \boldsymbol{u}(\boldsymbol{Y},t)}{\partial t}\right|_{\boldsymbol{Y}=\mathcal{A}^{-1}(\boldsymbol{x})} = \left.\frac{\partial \boldsymbol{u}(\boldsymbol{x},t)}{\partial t}\right|_{\boldsymbol{x}} + \boldsymbol{w}(\boldsymbol{x},t)\cdot\nabla\boldsymbol{u}(\boldsymbol{x},t), \quad \boldsymbol{x}\in\Omega_t,\ \boldsymbol{Y}\in\Omega_{ref} \tag{4}$$

and the domain velocity $\boldsymbol{w}(\boldsymbol{x},t) := \left.\frac{\partial \mathcal{A}(\boldsymbol{Y})}{\partial t}\right|_{\boldsymbol{Y}=\mathcal{A}^{-1}(\boldsymbol{x})} = \frac{\partial \boldsymbol{x}}{\partial t}$ for $\boldsymbol{x}\in\Omega_t$, $\boldsymbol{Y}\in\Omega_{ref}$ we rewrite the governing equations (1) into a formulation that takes explicitly into account

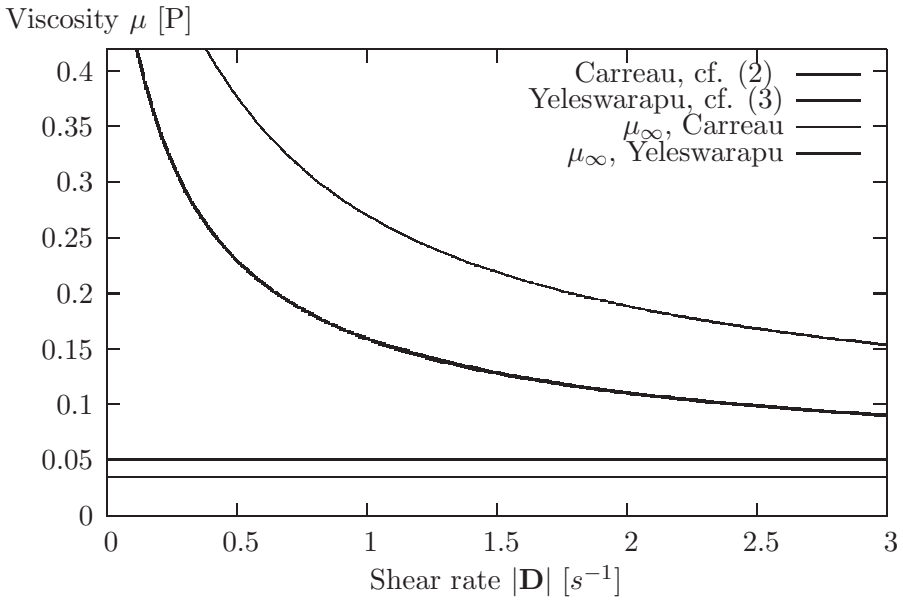

Figure 1: Shear-thinning viscosity (2), (3) for physiological blood parameters.

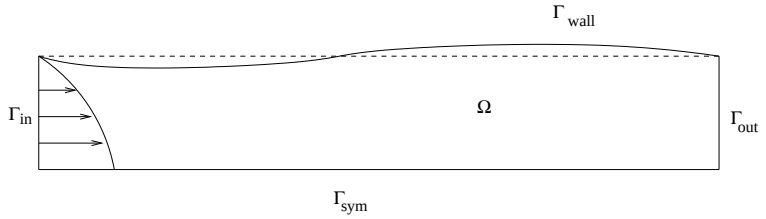

Figure 2: Computational domain geometry.

time-dependent behaviour of the domain, i.e.

$$\rho\left[\frac{\mathcal{D}^{\mathcal{A}}\boldsymbol{u}}{\mathcal{D}t} + ((\boldsymbol{u}-\boldsymbol{w})\cdot\bigtriangledown)\boldsymbol{u}\right] - \operatorname{div}\Big[2\mu(\mathbf{D}(\boldsymbol{u}))\ \mathbf{D}(\boldsymbol{u})\Big] + \bigtriangledown p = \boldsymbol{f} \tag{5}$$
$$\operatorname{div}\boldsymbol{u} = 0 \quad \text{on} \quad \Omega(\eta(t)).$$

Equation (5) is equipped with the initial and boundary conditions

$$\boldsymbol{u} = \boldsymbol{u}_0 \quad \text{with} \quad \operatorname{div}\boldsymbol{u}_0 = 0 \qquad \text{on} \quad \Omega_0, \tag{6}$$

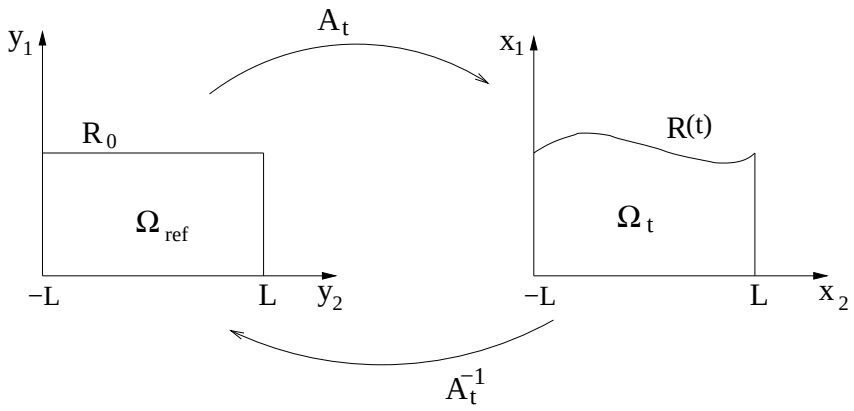

Figure 3: ALE-mapping $\mathcal{A}_t$ for a domain with moving boundary.

$$\left(\mathbf{T}(\boldsymbol{u},p)-\frac{1}{2}|\boldsymbol{u}|^2\mathbf{I}\right)\cdot\boldsymbol{n}=-P_{in}\ \mathbf{I}\cdot\boldsymbol{n}, \qquad \text{on} \quad \Gamma_{in},\ t\in(0,T), \tag{7}$$

$$\left(\mathbf{T}(\boldsymbol{u},p)-\frac{1}{2}|\boldsymbol{u}|^2\mathbf{I}\right)\cdot\boldsymbol{n}=-P_{out}\ \mathbf{I}\cdot\boldsymbol{n}, \qquad \text{on} \quad \Gamma_{out},\ t\in(0,T), \tag{8}$$

$$\frac{\partial u_1}{\partial x_2}=0, \quad u_2=0, \qquad \text{on} \quad \Gamma_{sym},\ t\in(0,T). \tag{9}$$

Conditions (7) and (8) are called the kinematical pressure conditions. The fluid velocity is coupled with the velocity of wall deformation by the so-called kinematical coupling condition

$$\boldsymbol{u}=\boldsymbol{w}:=\left(0,\frac{\partial\eta}{\partial t}\right)^T \quad \text{on} \quad \Gamma_{wall},\ t\in(0,T). \tag{10}$$

3 Generalized string model for the wall deformation

In order to model biological structure several models have been proposed in literature. For example, to model flow in a collapsible tubes a two-dimensional thin shell model can be used, see results of Wall et al. [16]. Recently Čanič et al. [6] developed a new one-dimensional model for arterial walls, the linearly viscoelastic cylindrical Koiter shell model, that is closed and rigorously derived by energy estimates, asymptotic analysis and homogenization techniques. The viscous fluid dissipation imparts long-term viscoelastic memory effects represented by higher order derivatives.

In the present work we will consider the *generalized string model* for vessel wall deformation. The original generalized string model, see [40], was valid only for radially symmetric domains with a constant reference radius R_0. In order to model stenotic occlusions we will extend this model and assume that the reference radius at rest R_0 depends on the longitudinal variable.

Let us consider a three-dimensional radially symmetric domain. We assume that the deformations are only in the radial direction and set $x_1 = z$ - longitudinal direction and

$x_2 = r$ - radial direction. The radial wall displacement, constant with respect to the angle θ, is defined as

$$\eta(z,t) = R(z,t) - R_0(z), \quad z \in (-L, L),\ t \in (0, T),$$

where $R(z,t)$ is the actual radius and $R_0(z)$ is the reference radius at rest. Since the actual radius of the compliant tube is given by $R(z,t) = R_0(z) + \eta(z,t)$, the reference radius R_0 and the actual radius R coincides for fixed solid domains and are dependent only on the spatial variable z. The assumption of radially symmetric geometry and radial displacement allow us to approximate the length of arc in the reference configuration by $dc_0 \approx R_0 d\theta$ and the length of the deformed arc as $dc \approx R d\theta$, see Fig. 4 and also [40]. Further, we assume that the gradient of displacement $\partial_z \eta$ is small, which implies the linear constitutive law (linear elasticity) of the vessel wall. The wall thickness is assumed to be small and constant. Moreover we approximate the infinitesimal surface S of Γ_{wall} in the following way $S \approx dc\, dl$.

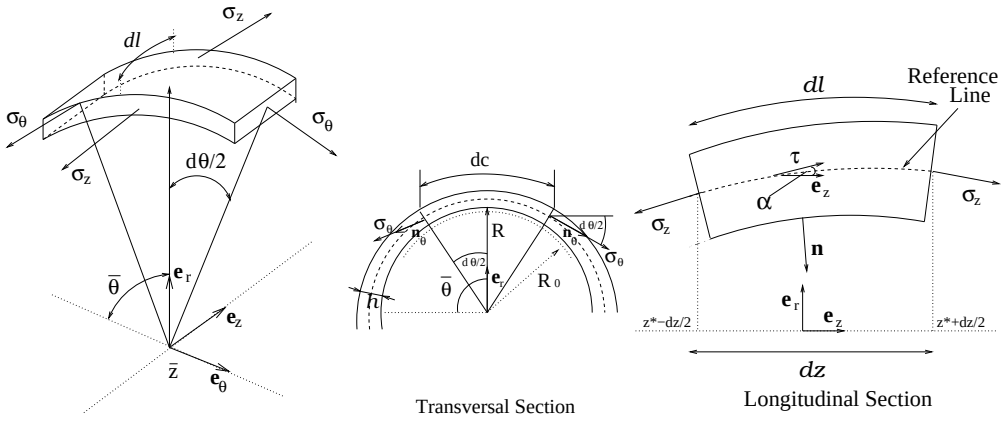

Figure 4: Small portion of vessel wall with physical characteristics [40].

The linear momentum law: $Force = Mass \times Acceleration$ is applied in the radial direction to obtain the equation for η.

$$Mass = \rho_w \hbar\, dc\, dl, \qquad Acceleration = \frac{\partial^2 R(z,t)}{\partial t^2} = \frac{\partial^2 \eta(z,t)}{\partial t^2}, \tag{11}$$

where ρ_w is the density of the wall and $\hbar$ its thickness.

Now we evaluate forces acting on the vessel wall. The tissue surrounding the vessel wall interacts with the vessel wall by exerting a constant pressure P_w. The resulting tissue force is $\boldsymbol{f}_{tissue} = -P_w \boldsymbol{n}\, dc\, dl \approx -P_w \boldsymbol{n} R\, d\theta\, dl$.

The forces from the fluid on Γ_{wall} are represented by the normal component of the Cauchy stress tensor $\boldsymbol{f}_{fluid} = -\mathbf{T}\,\boldsymbol{n}\, dc\, dl$, $\mathbf{T} = -p\mathbf{I} + 2\mu(\mathbf{D}(\boldsymbol{u}))\mathbf{D}(\boldsymbol{u})$. By summing the tissue and fluid forces we get the resulting external force acting on the vessel wall along the radial direction ($\boldsymbol{f}_{ext} = \boldsymbol{f}_{tissue} + \boldsymbol{f}_{fluid}$):

$$f_{ext}\Big|_{\Gamma_{wall}} = \boldsymbol{f}_{ext}\Big|_{\Gamma_{wall}} \cdot \boldsymbol{e}_r = (-\mathbf{T} - P_w\mathbf{I})\boldsymbol{n}\Big|_{\Gamma_{wall}} \cdot \boldsymbol{e}_r\, dc\, dl,$$

where $\boldsymbol{e}_r$ is the unit vector in the radial direction and $\boldsymbol{n} = \frac{1}{\sqrt{1+(\partial_z R)^2}}(-\partial_z R, 1)$ the unit outward normal to the boundary Γ_{wall}. We transform this force from the Eulerian to the Lagrangian coordinates, see, e.g., [24] for more details.

$$f_{ext}\Big|_{\Gamma^0_{wall}} = -(\tilde{\mathbf{T}} + \tilde{P_w}\mathbf{I})\tilde{\boldsymbol{n}}\Big|_{\Gamma^0_{wall}} \cdot \boldsymbol{e}_r \frac{R\sqrt{1+(\partial_z R)^2}}{R_0\sqrt{1+(\partial_z R_0)^2}} dc_0\, dl_0,$$

here $\boldsymbol{n}(x) = \tilde{\boldsymbol{n}}(\tilde{x}),\ x = (z, R(z,t)) \in \Gamma_{wall}, \tilde{x} = (z, R_0(z)) \in \Gamma^0_{wall}$. The term $\frac{R\sqrt{1+(\partial_z R)^2}}{R_0\sqrt{1+(\partial_z R_0)^2}}$ arrives from the transformation to the Lagranian coordinates, in particular we have the transformation of the curve $\Gamma_{wall}(t) = \{(z, R(z,t)), z \in (-L, L)\}$ to the curve $\Gamma^0_{wall} = \{(z, R_0(z)), z \in (-L, L)\}$.

The internal forces acting on the vessel portion are due to the circumferential stress $\boldsymbol{\sigma}_\theta$ (constant with respect to the angle) and the longitudinal stress $\boldsymbol{\sigma}_z$. Both stresses are directed along the normal to the surface to which they act. Let us denote $\sigma_\theta = \boldsymbol{\sigma}_\theta \cdot \boldsymbol{n}$. Further the longitudinal stress $\boldsymbol{\sigma}_z$ is parallel to tangent, i.e. $\boldsymbol{\sigma}_z = \pm\sigma_z\boldsymbol{\tau}$. The sign is positive if the versus of the normal to the surface, on which $\boldsymbol{\sigma}_z$ is acting, is the same as those chosen for $\boldsymbol{\tau}$.

We have $f_{int} = (\boldsymbol{f}_\theta + \boldsymbol{f}_z) \cdot \boldsymbol{e}_r$ and

$$\begin{aligned}
\boldsymbol{f}_\theta \cdot \boldsymbol{e}_r &= \Big[\boldsymbol{\sigma}_\theta\Big(\bar{\theta} + \frac{d\theta}{2}\Big) + \boldsymbol{\sigma}_\theta\Big(\bar{\theta} - \frac{d\theta}{2}\Big)\Big] \cdot \boldsymbol{e}_r \hbar\, dl = 2|\sigma_\theta| cos\Big(\frac{\pi}{2} + \frac{d\theta}{2}\Big)\hbar\, dl \\
&= -2|\sigma_\theta| \sin\left(\frac{d\theta}{2}\right)\hbar\, dl \approx -|\sigma_\theta|\hbar\ d\theta\ dl = -E\frac{\eta}{R_0}\hbar\ d\theta\ dl, \\
\boldsymbol{f}_z \cdot \boldsymbol{e}_r &= \Big[\boldsymbol{\sigma}_z\Big(z^* + \frac{dz}{2}\Big) + \boldsymbol{\sigma}_z\Big(z^* - \frac{dz}{2}\Big)\Big] \cdot \boldsymbol{e}_r \hbar\, dc \\
&= \frac{\boldsymbol{\tau}(z^* + \frac{dz}{2}) - \boldsymbol{\tau}(z^* - \frac{dz}{2})}{dz} \cdot \boldsymbol{e}_r \hbar |\sigma_z|\, dz\, dc \\
&\approx |\sigma_z|\Big[\frac{d\boldsymbol{\tau}}{dz}(z^*)\Big] \cdot \boldsymbol{e}_r \hbar\, dz\, dc \\
&\approx \left(\frac{\partial^2\eta}{\partial z^2} + \frac{\partial^2 R_0}{\partial z^2}\right)\left[1 + \left(\frac{\partial R_0}{\partial z}\right)^2\right]^{-1} \boldsymbol{n} \cdot \boldsymbol{e}_r |\sigma_z| \hbar dz\, dc.
\end{aligned}$$

Here we have used the following properties. According to the linear elasticity assumption the stress tensor $\boldsymbol{\sigma}_\theta$ is proportional to the relative circumferential prolongation, i.e.

$$\boldsymbol{\sigma}_\theta = E\frac{2\pi(R - R_0)}{2\pi R_0} = E\frac{\eta}{R_0}, \quad E \text{ is Young's modulus of elasticity.}$$

To evaluate the longitudinal force we have used the following result, that is a generalization of an analogous lemma from [40].

Lemma. *If $\frac{\partial\eta}{\partial z}$ is small then*

$$\frac{d\boldsymbol{\tau}}{dz}(z^*) \approx \left(\frac{\partial^2\eta}{\partial z^2} + \frac{\partial^2 R_0}{\partial z^2}\right)\left[1 + \left(\frac{\partial R_0}{\partial z}\right)^2\right]^{-1} \boldsymbol{n}.$$

Proof: Let a parametric curve $\mathbf{c}$ be defined at each t on the plane (z,r) by

$$\mathbf{c}:\mathbb{R}\to\mathbb{R}^2,\ z\to(c_1(z),c_2(z))=(z,R(z,t))=(z,R_0(z,t)+\eta(z,t)),$$

and $\boldsymbol{\tau}$, $\boldsymbol{n}$, κ denote the tangent, the normal and the curvature of $\mathbf{c}$, respectively. Then according to the Serret-Frenet formula [40] we have

$$\frac{d\tau}{dz}(z)=\left|\frac{d\mathbf{c}}{dz}(z)\right|\kappa(z)\tilde{\boldsymbol{n}}(z).$$

Here $\tilde{\boldsymbol{n}}=\pm\boldsymbol{n}$ is the normal oriented towards the center of curvature. Furthermore since we assume $\frac{\partial\eta}{\partial z}$ to be small, we have

$$\begin{aligned}\left|\frac{d\mathbf{c}}{dz}(z)\right| &= \left[1+\left(\frac{\partial R}{\partial z}\right)^2\right]^{1/2}\approx\left[1+\left(\frac{\partial R_0}{\partial z}\right)^2\right]^{1/2}\quad\text{and}\\ \kappa &= \left|\frac{dc_1}{dz}\frac{d^2c_2}{dz^2}-\frac{dc_2}{dz}\frac{d^2c_1}{dz^2}\right|\left|\frac{d\mathbf{c}}{dz}\right|^{-3}=\left|\frac{\partial^2R}{\partial z^2}\right|\left[1+\left(\frac{\partial R}{\partial z}\right)^2\right]^{-\frac{3}{2}}\\ &\approx \left|\frac{\partial^2R_0+\partial^2\eta}{\partial z^2}\right|\left[1+\left(\frac{\partial R_0}{\partial z}\right)^2\right]^{-\frac{3}{2}}.\end{aligned}$$

Since the sign of $\frac{\partial^2R}{\partial z^2}$ determines the convexity of curve, $\tilde{\boldsymbol{n}}=sign\left(\frac{\partial^2R}{\partial z^2}\right)\boldsymbol{n}$, we obtain the desired result. ■

Now we use the assumption of the incompressibility of material; the volume of the infinitesimal portion remains constant under the deformation: $\hbar dcdl=\hbar dc_0dl_0$. Using this assumption the internal forces can be expressed as

$$f_{int}\approx\left\{-E\frac{\eta}{RR_0}+\left(\frac{\partial^2\eta}{\partial z^2}+\frac{\partial^2R_0}{\partial z^2}\right)\left[1+\left(\frac{\partial R_0}{\partial z}\right)^2\right]^{-1}\boldsymbol{n}\cdot\boldsymbol{e}_r|\sigma_z|\frac{dz}{dl}\right\}\hbar\,dc_0dl_0.$$

Moreover, we use the fact that $\boldsymbol{n}\cdot\boldsymbol{e}_r=1/\sqrt{1+(\partial_zR)^2}\approx1/\sqrt{1+(\partial_zR_0)^2}$, and

$$\frac{dz}{dl}\approx\cos(\measuredangle(\boldsymbol{e}_z,\boldsymbol{\tau}))=\boldsymbol{e}_z\cdot\boldsymbol{\tau}\approx1/\sqrt{1+(\partial_zR_0)^2},$$

compare Fig. 4.

Summing up all contributions of balancing forces acting on the infinitesimal portion of Γ_{wall} we obtain from the linear momentum law (11) using the transformation to Γ^0_{wall}

$$\begin{aligned}\Bigg\{\rho_w\hbar\frac{\partial^2\eta}{\partial t^2}-|\sigma_z|\frac{\left(\frac{\partial^2\eta}{\partial z^2}+\frac{\partial^2R_0}{\partial z^2}\right)}{\left[1+\left(\frac{\partial R_0}{\partial z}\right)^2\right]^2}\hbar+E\hbar\frac{\eta}{R_0R}\\ +(\tilde{\mathbf{T}}+\tilde{P_w}\mathbf{I})\tilde{\boldsymbol{n}}\cdot\boldsymbol{e}_r\frac{R\sqrt{1+\left(\frac{\partial(R_0+\eta)}{\partial z}\right)^2}}{R_0\sqrt{1+(\frac{\partial R_0}{\partial z})^2}}\Bigg\}R_0d\theta\,dl_0 &= o(d\theta\,dl_0).\end{aligned}$$

Thus by dividing the above equation by $\rho_w \hbar\, R_0\, d\theta\, dl_0$ and passing to the limit for $d\theta \to 0$, $dl_0 \to 0$ we obtain the so called *vibrating string model*. Adding a damping term $-c\partial^3_{tzz}\eta$ (or $-c\partial^5_{tzzzz}\eta$) $c > 0$ at the left hand side we get the *generalized string model* for radially symmetric domains with non-constant reference radius $R_0(z)$

$$\left[\frac{\partial^2\eta}{\partial t^2} - \frac{|\sigma_z|}{\rho_w}\frac{\left(\frac{\partial^2\eta}{\partial z^2} + \frac{\partial^2 R_0}{\partial z^2}\right)}{\left[1+(\partial_z R_0)^2\right]^2} + \frac{E\eta}{\rho_w R_0(R_0+\eta)} - c\frac{\partial^3\eta}{\partial t\partial^2 z}\right](z,t) = \tag{12}$$

$$\left[-(\tilde{\mathbf{T}} + \tilde{P}_w\mathbf{I})\tilde{\boldsymbol{n}}\right](z, R_0(z)) \cdot \boldsymbol{e}_r \frac{(R_0+\eta)(z,t)}{R_0(z)\rho_w\hbar}\frac{\sqrt{1+(\partial_z R_0 + \partial_z\eta)^2}}{\sqrt{1+(\partial_z R_0)^2}}.$$

The generalized string model for structure (12) is completed with the initial and boundary conditions

$$\eta = 0, \quad \frac{\partial\eta}{\partial t} = \boldsymbol{u}_0|_{\Gamma^0_{wall}} \cdot \boldsymbol{e}_r \qquad \text{on} \quad \Gamma^0_{wall}, \tag{13}$$

$$\eta(-L,t) = \eta_1, \quad \eta(L,t) = \eta_2, \qquad \text{for} \quad t \in (0,T). \tag{14}$$

Let us point out that the coupling of fluid and structure is realized by the kinematical and dynamical coupling conditions. The dynamical coupling is represented by the continuity of stresses, i.e. the fluid forces acting on the structure are due to fluid stress tensor at the right hand side of the structure equation (12). The kinematical coupling represents the continuity of velocities at the moving boundaries, which is the condition (10).

4 Fluid-structure interaction methods

In what follows we describe two numerical schemes for coupling the fluid and the structure. The first approach, called *the global iterative method*, is based on the global iterations with respect to the domain geometry. This method belongs to the strong coupling-type methods. In the second approach, *the kinematical splitting*, the structure equation (12) is splitted into two parts, which are solved consequently. Using this splitting, no additional iterations between the fluid and the structure are necessary. The second method belongs to the class of weakly coupled methods.

4.1 Strong coupling: global iterative method

Assume that the domain deformation $\eta = \eta^{(k)}$ is a given function, take $\eta^{(0)} = \eta(\cdot,0)$. The vector $(\boldsymbol{u}^{(k+1)}, p^{(k+1)}, \eta^{(k+1)})$ is obtained as a solution of (1), (12) for all $x \in \Omega(\eta^{(k)})$, $x_1 \in (-L,L)$ and all $t \in (0,T)$. Instead of condition (10) we use

$$u_2(x_1,x_2,t) = \frac{\partial\eta^{(k)}}{\partial t}(x_1,t) = w_2(x_1,x_2,t), \;\; u_1(x_1,x_2,t) = 0 \qquad \text{on } \Gamma^{(k)}_{wall}(t), \tag{15}$$

where $\Gamma_{wall}^{(k)}(t) = \{(x_1, x_2);\ x_2 = R_0(x_1) + \eta^{(k)}(x_1, t),\ x_1 \in (-L, L)\}$, $t \in (0, T)$ and $\boldsymbol{w}$ is the velocity of mesh movement related to smoothing the grid after moving its boundary (we allow just movement in the x_2 direction, x_1 direction is neglected), see also [51].

Further we linearize the equation (12) replacing the non-linear term on its left hand side by $E\eta/(\rho_w(R_0+\eta^{(k)})R_0)$. In order to decouple (1) or (5) and (12) we evaluate the forcing term at the right hand side of (12) at the old time step t^{n-1}, see also Fig 6. Convergence of this global method was verified experimentally. Our extensive numerical experiments show fast convergence of domain deformation, two iteration of domain deformation differ about $10^{-4}cm$ (for e.g., $R_0 = 1cm$) pointwisely after few, about 5 iterations. As an example we have depicted in Figure 3 a deformed vessel wall after 1, 2, 3 and 9 global iterations at the same time $T = 0.36s$. It illustrates that the vessel wall converges to one curve and does not change significantly already after second iteration, see Fig. 5. Theoretical proof of the convergence $\eta^{(k)} \to \eta$ can be obtained by means of the Schauder fixed point theorem, cf. [25] and the following subsection.

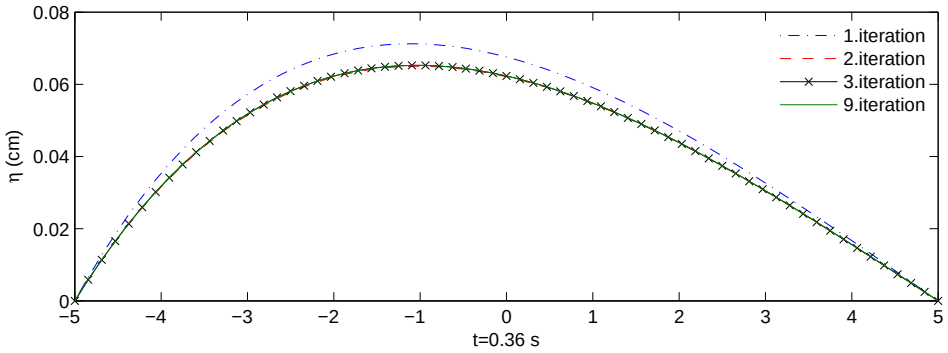

Figure 5: Several iterations of the wall deformation η at time $t = 0.36s$, after a few iterations curves coincide. Computed for the Carreau model with $Re = 40$, cf. (49).

4.1.1 Existence of a weak solution to the coupled problem

In the recent years the well-posedness of fluid-structure interaction is being extensively studied. In particular, the well-possedness of the mathematical model describing the Newtonian fluid flow in compliant vessels has been studied in [6, 7, 13, 23, 25, 47], see also [4, 5] for related results. In [47] local existence in time of strong solutions is shown, provided the initial data are sufficiently small. Cheng, Shkoller and Coutand [9, 11] studied coupled problem consisting of viscous incompressible fluid and elastic solid shell. Mathematically, the shell encloses the fluid and creates a time-dependent boundary of viscous fluid. In [9] Cheng and Shkoller proved local (in time) existence and uniqueness of regular solutions. For three-dimensional problems in addition some smallness of shell thickness has to be assumed. The difficulty of the coupled model lies in a parabolic-hyperbolic coupling of viscous fluid and hyperbolic structure. A new idea presented in their recent works [10, 11, 12] is based on introducing a functional framework that scales

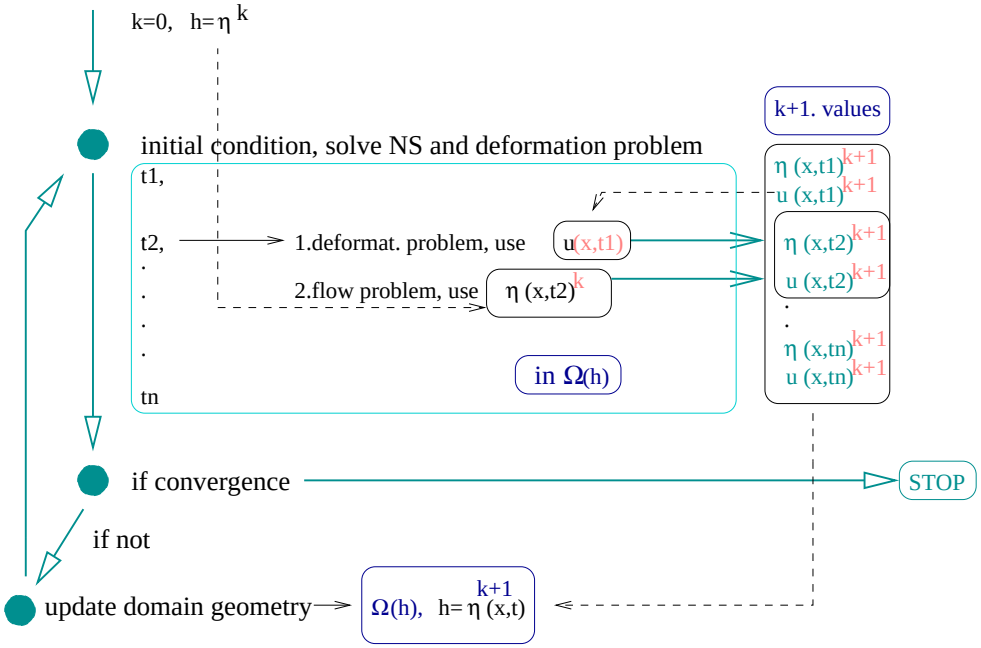

Figure 6: The sketch of the global iterative method.

in a hyperbolic fashion and is thus driven by the elastic structure. The problem has been reformulated in the Lagrangian coordinates.

In contrast to these local existence and uniqueness results for regular solutions we can find already several results on global existence of weak solutions. Recently, Padula et al. [23] showed the global existence in time of weak solutions when initial data are sufficiently close to equilibrium. If no restriction on initial data is assumed, then weak solutions exist as long as the elastic wall does not touch the rigid bottom [23]. In [22] uniqueness and continuous dependence on initial data for weak solutions has been studied.

Similarly, in [7] Chambole et al. proved the global existence of weak solutions until a contact of the viscoelastic and the rigid boundary, see also [20] for the existence result of stationary solution and the elastic Saint-Venant-Kirchhoff material and [44] for related results.

In [25] we have proved the existence of a weak solution of fully coupled fluid-structure interaction problem between the non-Newtonian shear-thickening fluid and linear viscoelastic structure. In order to obtain enough regular η we need to regularize the structure equation (12) with η_{txxxx} instead of η_{txx}.

Now, assuming that η is enough regular (see below) and taking into account the results from [7] we can define functional spaces that give sense to the trace of velocity from $W^{1,p}(\Omega(\eta(t)))$ and thus define the weak solution of the problem. We assume that $R_0 \in C_0^2(0,L)$. Note that p is the exponent of the polynomial viscosity function, see, e.g., (2). In [25] more general non-Newtonian models with a polynomially growing potential of the stress tensor have been analyzed as well .

Definition 4.1 [Weak formulation]
We say that $(\boldsymbol{u}, \eta)$ is a weak solution of (1), (12), (10) with the initial and boundary conditions (6), (7), (8), (9), (13), (14) on $[0,T)$ if the following conditions hold

- $\boldsymbol{u} \in L^p(0,T; W^{1,p}(\Omega(\eta(t)))) \cap L^\infty(0,T; L^2(\Omega(\eta(t))))$
- $\eta \in W^{1,\infty}(0,T; L^2(-L,L)) \cap H^1(0,T; H_0^2(-L,L))$
- $\operatorname{div} \boldsymbol{u} = 0$ a.e. on $\Omega(\eta(t))$
- $\boldsymbol{u} = (0, \eta_t)$ for a.e. $\boldsymbol{x} \in \Gamma_w(t),\ t \in (0,T)$,

$$
\begin{aligned}
&\int_0^T \int_{\Omega(\eta(t))} \left\{ -\rho \boldsymbol{u} \cdot \frac{\partial \boldsymbol{\varphi}}{\partial t} + 2\mu(|(\boldsymbol{u})|)\mathbf{D}(\boldsymbol{u})\mathbf{D}(\boldsymbol{\varphi}) + \rho \sum_{i,j=1}^{2} u_i \frac{\partial u_j}{\partial x_i} \boldsymbol{\varphi}_j \right\} d\boldsymbol{x}\, dt \\
&+ \int_0^T \int_0^{R_0(L)} \left(P_{out} - \frac{\rho}{2} |u_1|^2 \right) \varphi_1(L, x_2, t)\, dx_2\, dt \\
&- \int_0^T \int_0^{R_0(0)} \left(P_{in} - \frac{\rho}{2} |u_1|^2 \right) \varphi_1(-L, x_2, t)\, dx_2\, dt \\
&+ \int_0^T \int_{-L}^{L} P_w \varphi_2(x_1, R_0(x_1) + \eta(x_1,t), t) - a \frac{\partial^2 R_0}{\partial x_1^2} \xi\, dx_1\, dt \\
&+ \int_0^T \int_{-L}^{L} -\frac{\partial \eta}{\partial t} \frac{\partial \xi}{\partial t} + c\, \frac{\partial^3 \eta}{\partial x_1^2 \partial t} \frac{\partial^2 \xi}{\partial x_1^2} + a \frac{\partial \eta}{\partial x_1} \frac{\partial \xi}{\partial x_1} + b\eta\, \xi\, dx_1\, dt \ = \ 0
\end{aligned}
\tag{16}
$$

for every test functions

$$
\begin{aligned}
&\boldsymbol{\varphi}(x_1, x_2, t) \in H^1(0,T; W^{1,p}(\Omega(\eta(t)))) \text{ such that} \\
&\operatorname{div} \boldsymbol{\varphi} = 0 \text{ a.e on } \Omega(\eta(t)), \\
&\varphi_2|_{\Gamma_w(t)} \in H^1(0,T; H_0^2(\Gamma_w(t))) \quad \text{and} \\
&\xi(x_1, t) = \tilde{E} \rho\, \boldsymbol{\varphi}_2(x_1, R_0(x_1) + \eta(x_1,t), t),
\end{aligned}
$$

where $\tilde{E}$ is a given constant depending on the structural material properties.

Theorem 4.1 (Existence of a weak solution [25])**.**
Let $p \geq 2$. Assume that the boundary data fulfill $P_{in} \in L^{p'}(0,T; L^2(0, R_0(0)))$, $P_{out} \in L^{p'}(0,T; L^2(0, R_0(L)))$, $P_w \in L^{p'}(0,T; L^2(-L,L))$, $\frac{1}{p} + \frac{1}{p'} = 1$. Furthermore, assume that

the viscous stress tensor τ has a potential $\mathcal{U} \in C^2(\mathbb{R}^{2\times 2})$ satisfying the following conditions

$$\frac{\partial \mathcal{U}(\eta)}{\partial \eta_{ij}} = \tau_{ij}(\eta) \tag{17}$$

$$\mathcal{U}(\mathbf{0}) = \frac{\partial \mathcal{U}(\mathbf{0})}{\partial \eta_{ij}} = 0 \tag{18}$$

$$\frac{\partial^2 \mathcal{U}(\eta)}{\partial \eta_{mn}\partial \eta_{rs}}\xi_{mn}\xi_{rs} \geq C_1\ (1+|\eta|)^{p-2}|\xi|^2 \tag{19}$$

$$\left|\frac{\partial^2 \mathcal{U}(\eta)}{\partial \eta_{ij}\partial \eta_{kl}}\right| \leq C_2(1+|\eta|)^{p-2}. \tag{20}$$

Then there exists a weak solution $(\boldsymbol{u}, \eta)$ of the problem (1), (12), (10) with the initial and boundary conditions (6), (7), (8), (9), (13), (14) such that

i) $\boldsymbol{u} \in L^p(0,T; W^{1,p}(\Omega(\eta(t)))) \cap L^\infty(0,T; L^2(\Omega(\eta(t))))$,
$\eta \in W^{1,\infty}(0,T; L^2(-L,L)) \cap H^1(0,T; H_0^2(-L,L))$
ii) $\boldsymbol{u} = (0, \eta_t)$ *for a.e.* $\boldsymbol{x} \in \Gamma_w(t),\ t \in (0,T)$
iii) $\boldsymbol{u}$ *satisfies the condition* $div\,\boldsymbol{u} = 0$ *a.e on* $\Omega(\eta(t))$ *and (16) holds.*

The proof of existence is realized in several steps:

a) Approximation of the solenoidal spaces on a moving domain by the artificial compressibility approach: ε - approximation

$$\varepsilon\left(\frac{\partial p_\varepsilon}{\partial t} - \Delta p_\varepsilon\right) + \operatorname{div} \boldsymbol{v}_\varepsilon = 0 \quad \text{in } \Omega(\eta^{(k)}), \tag{21}$$

$$\frac{\partial p_\varepsilon}{\partial \boldsymbol{n}} = 0 \ \text{ on } \ \partial\Omega(\eta^{(k)}), \quad \varepsilon > 0.$$

b) Splitting the boundary conditions (10), (12) by introducing the semi-pervious boundary: κ - approximation.

$$\left[\mu(|e(\boldsymbol{v})|)\left\{-\left(\frac{\partial v_2}{\partial x_1} + \frac{\partial v_1}{\partial x_2}\right)\frac{\partial h}{\partial x_1} + 2\frac{\partial v_2}{\partial x_2}\right\} - p + P_w\right](\bar{x}, t) \tag{22}$$

$$-\frac{\rho}{2}v_2\Big(v_2(\bar{x},t) - \frac{\partial \eta^{(k)}}{\partial t}(x_1,t)\Big) = \rho\kappa\Big(\frac{\partial \eta}{\partial t}(x_1,t) - v_2(\bar{x},t)\Big)$$

and

$$-\tilde{E}\left[\frac{\partial^2 \eta}{\partial t^2} - a\frac{\partial^2 \eta}{\partial x_1^2} + b\eta + c\frac{\partial^5 \eta}{\partial t \partial x_1^4} - a\frac{\partial^2 R_0}{\partial x_1^2}\right](x_1,t) \tag{23}$$

$$= \kappa\Big(\frac{\partial \eta}{\partial t}(x_1,t) - v_2(\bar{x},t)\Big) \qquad \bar{x} = (x_1, \eta^{(k)}(x_1,t)),\ x_1 \in (-L,L)$$

with $\kappa \gg 1$. For finite κ the boundary Γ_w is partly permeable, but letting $\kappa \to \infty$ it becomes impervious. In fact, we can prove the existence of solution if $\kappa \to \infty$ and thus we get the original boundary condition.

c) Transformation of the weak formulation on a time dependent domain $\Omega(\eta(t))$ to a fixed reference domain $D = (-L, L) \times (0, 1)$ using a given domain deformation $\eta = \eta^{(k)}$: k - approximation.

The (κ, ε)-approximated problem is defined on a moving domain depending on function $h = R_0 + \eta^{(k)}$. We will transform it to a fixed rectangular domain and set

$$\begin{aligned} \boldsymbol{v}(y_1, y_2, t) &\stackrel{\text{def}}{=} \boldsymbol{u}(y_1, h(y_1, t)y_2, t) \\ q(y_1, y_2, t) &\stackrel{\text{def}}{=} \rho^{-1} p(y_1, h(y_1, t)y_2, t) \\ \sigma(y_1, t) &\stackrel{\text{def}}{=} \frac{\partial \eta}{\partial t}(y_1, t) \end{aligned} \tag{24}$$

for $y \in D = \{(y_1, y_2);\ -L < y_1 < L,\ 0 < y_2 < 1\}$, $0 < t < T$.

d) Limiting process for $\varepsilon \to 0,\ \kappa \to \infty$ and $k \to \infty$, respectively.

We firstly show the existence of weak solutions of stationary problems obtained by time discretization. Furthermore, we derive suitable a priori estimates for piecewise approximations in time. By using the theory of monotone operators, the Minty-Browder theorem and the compactness arguments due to the Lions-Aubin lemma, we can show the convergence of time approximations to its weak unsteady solution. Thus we obtain the existence of a weak solution to the (κ, ε, k) - approximate problem. The next step are the limiting processes for κ and ε. First of all we show the limiting process in $\varepsilon \to 0$ since necessary a priori estimates obtained by means of the energy method are independent on ε. In order to realize the limiting process in κ; $\kappa \to \infty$, we however need new a priori estimates and show the semi-continuity in time. Thus, letting $\varepsilon \to 0$ and $\kappa \to \infty$ we obtain the existence of weak solution to the $k-$approximate problem depending only on the approximation of domain deformation $h(x_1, t) = R_0(x_1) + \eta^{(k)}(x_1, t)$. The final limiting process with respect to the domain deformation, i.e. for $k \to \infty$ will be realized by the Schauder fixed point arguments for a regularized problem and consequently by passing to the limit with the regularizing parameter. This will yield the existence of at least one weak solution of the fully coupled unsteady fluid-structure interaction between the non-Newtonian shear-dependent fluid and the viscoelastic string.

The existence result from [25] is the generalization of the results of Filo and Zaušková [13] where the Newtonian fluids were considered. In [13] the generalized string equation with a third order regularizing term was considered, but the final limiting step for $k \to \infty$ was open.

4.2 Weak coupling: kinematical splitting algorithm

First, let us rewrite the generalized string model (12) in the following way

$$\frac{\partial^2 \eta}{\partial t^2} - a\frac{\partial^2 \eta}{\partial x_1^2} + b\eta - c\frac{\partial^3 \eta}{\partial t \partial x_1^2} = -\frac{(\mathbf{T} + P_w\ \mathbf{I}) \cdot \boldsymbol{n} \cdot \boldsymbol{e}_r}{\rho_w \hbar} + a\frac{\partial^2 R_0}{\partial x_1^2} \quad \text{on} \quad \Gamma_{wall}(t) \tag{25}$$

or

$$\frac{\partial^2\eta}{\partial t^2}-a\frac{\partial^2\eta}{\partial x_1^2}+b\eta-c\frac{\partial^3\eta}{\partial t\partial x_1^2}=-\frac{(\tilde{\mathbf{T}}+\tilde{P}_w\,\mathbf{I})\cdot\tilde{\boldsymbol{n}}\cdot\boldsymbol{e}_r}{\rho_w\hbar}\frac{R}{R_0}\frac{\sqrt{1+(\partial_{x_1}R)^2}}{\sqrt{1+(\partial_{x_1}R_0)^2}}+a\frac{\partial^2R_0}{\partial x_1^2}\quad\text{on}\quad\Gamma^0_{wall}\,. \tag{26}$$

Here the parameters are defined as follows

$$a=\frac{|\sigma_{x_1}|}{\rho_w}\left[1+\left(\frac{\partial R_0}{\partial x_1}\right)^2\right]^{-2},\quad b=\frac{E}{\rho_w R_0(R_0+\eta)},\quad c=\frac{\gamma}{\rho_w\hbar}. \tag{27}$$

Recall that E is the Young modulus, $\hbar$ the thickness of the vessel wall, ρ_w its density, γ is a positive viscoelastic constant and $|\sigma_{x_1}|$ magnitude of the stress tensor component in the longitudinal direction, cf. also Subsection 5.3 for typical physiological values. The kinematical splitting algorithm is based on the kinematical coupling condition

$$\boldsymbol{u}=\boldsymbol{w}:=\left(0,\frac{\partial\eta}{\partial t}\right)\quad\text{on}\quad\Gamma^0_{wall} \tag{28}$$

and special splitting of the structure equation into the hyperbolic and parabolic part. We define the operator A that includes the fluid solver for (5) and the viscoelastic part of structure equation

$$\textbf{A}\ \textbf{operator}\ (\text{hydrodynamic})\begin{cases}\text{fluid solver }(\boldsymbol{u},p),\\ \xi:=u_2|_{\Gamma_{wall}},\\ \dfrac{\partial\xi}{\partial t}=c\dfrac{\partial^2\xi}{\partial {x_1}^2}+H(\boldsymbol{u},p)\end{cases} \tag{29}$$

and the operator B for purely elastic load of the structure

$$\textbf{B}\ \textbf{operator}\ (\text{elastic})\begin{cases}\dfrac{\partial\eta}{\partial t}=\xi,\\ \dfrac{\partial\xi}{\partial t}=a\dfrac{\partial^2\eta}{\partial {x_1}^2}-b\eta+H(R_0),\end{cases} \tag{30}$$

where

$$H(\boldsymbol{u},p):=-\frac{(\tilde{\mathbf{T}}+\tilde{P}_w\mathbf{I})\cdot\tilde{\boldsymbol{n}}\cdot\boldsymbol{e}_r}{\rho_w\hbar}\frac{(R_0+\eta)}{R_0}\frac{\sqrt{1+(\partial_{x_1}R)^2}}{\sqrt{1+(\partial_{x_1}R_0)^2}},\quad H(R_0):=a\frac{\partial^2R_0}{\partial x_1^2}\,. \tag{31}$$

Here we note that the coupling condition allowed us to rewrite the hydrodynamic part of structure equation in the terms of wall velocity ξ. Time discretization of our problem is done in the following way: from the fluid equation we compute new velocities $\boldsymbol{u}^{n+1}$ and pressures p^{n+1} for $x^n\in\Omega^n$ (i.e. Ω_t for $t=t^n$). Note that $\tilde{\boldsymbol{u}}^{n+1}=\boldsymbol{u}^{n+1}\circ\mathcal{A}_{t^{n+1}}\circ\mathcal{A}_{t^n}^{-1}$ and $\tilde{p}^{n+1}=p^{n+1}\circ\mathcal{A}_{t^{n+1}}\circ\mathcal{A}_{t^n}^{-1}$, where $\mathcal{A}_{t^n}$ is the ALE-mapping from a reference domain Ω_{ref} onto Ω^n. Then we continue with computing of the wall velocity $\xi^{n+\frac{1}{2}}$ from the

hydrodynamic part of structure equation (29). Further on we proceed with the operator B and compute new wall displacement η^{n+1} and new wall velocity ξ^{n+1}. Finally, knowing η^{n+1} the geometry is updated from Ω^n to Ω^{n+1} and new values of fluid velocity $\boldsymbol{u}^{n+1}$ and pressure p^{n+1} are transformed onto Ω^{n+1}. In order to update the domain Ω^n we need to define the grid velocity $\boldsymbol{w}$. First, we set $\boldsymbol{w}|_{\Gamma_{wall}} = \xi^{n+1}$. In order to prescribe the grid velocity also inside Ω we can solve an auxiliary problem, cf., e.g., [15] or interpolate $\boldsymbol{w}$. Consequently, we get $\boldsymbol{w}^{n+1} = \partial \boldsymbol{x}/\partial t$, $\boldsymbol{x} \in \Omega^{n+1}$.

4.2.1 Stability analysis

In what follows we will briefly describe stability analysis of the semi-discrete scheme for the kinematical coupling approach. More details on the derivation can be found in [28]. Now, let us consider the weak formulation of the fluid equation and set for the test function $\boldsymbol{u}$. Integrating over Ω^n and approximating the time derivative by the backward Euler method the operator A yields the following equation for new intermediate velocities $\tilde{\boldsymbol{u}}^{n+1}$, $\xi^{n+\frac{1}{2}}$

$$
\begin{aligned}
&\int_{\Omega^n} \tilde{\boldsymbol{u}}^{n+1} \cdot \frac{\tilde{\boldsymbol{u}}^{n+1} - \boldsymbol{u}^n}{\Delta t}\, \mathrm{d}\omega + \frac{2}{\rho}\int_{\Omega^n} \mu(|\mathbf{D}(\tilde{\boldsymbol{u}}^{n+1})|)\, \mathbf{D}(\tilde{\boldsymbol{u}}^{n+1}) : \mathbf{D}(\tilde{\boldsymbol{u}}^{n+1})\, \mathrm{d}\omega \\
&+\frac{1}{2}\int_{\Omega^n} |\tilde{\boldsymbol{u}}^{n+1}|^2 \mathrm{div}\, \boldsymbol{w}^n\, \mathrm{d}\omega \quad = \quad -\rho_w \hbar \int_{\Gamma^0_{wall}} \left[\frac{\xi^{n+\frac{1}{2}} - \xi^n}{\Delta t}\right] \xi^{n+\frac{1}{2}}\, \mathrm{d}l_0 \\
&-\rho_w \hbar c \int_{\Gamma^0_{wall}} \left[\frac{\partial \xi^{n+\frac{1}{2}}}{\partial x_1}\right]^2 \mathrm{d}l_0 - \int_{\Gamma^n_{wall}} \frac{\tilde{P}_w(t^{n+1})\, \tilde{u}_2^{n+1}}{\sqrt{1+(\partial_{x_1} R_0)^2}}\, \mathrm{d}l \; + \int_{\Omega^n} \tilde{\boldsymbol{u}}^{n+1} \cdot \boldsymbol{f}^{n+1}\, \mathrm{d}\omega \\
&+ \int_0^{R_0} P_{in}(t^{n+1}) \tilde{u}_1^{n+1}|_{x_1=0}\, \mathrm{d}x_2 - \int_0^{R_0} P_{out}(t^{n+1}) \tilde{u}_1^{n+1}|_{x_1=L}\, \mathrm{d}x_2. \qquad (32)
\end{aligned}
$$

Moreover, we have $\mathrm{div}\, \tilde{\boldsymbol{u}}^{n+1} = 0$ in Ω^n. The operator B is discretized in time via the Crank-Nicolson scheme, i.e.

$$
\begin{aligned}
\frac{\eta^{n+1} - \eta^n}{\Delta t} &= \frac{1}{2}\big(\xi^{n+1} + \xi^{n+\frac{1}{2}}\big)\,, \qquad (33)\\
\frac{\xi^{n+1} - \xi^{n+\frac{1}{2}}}{\Delta t} &= \frac{a}{2}\big(\eta^{n+1}_{x_1x_1} + \eta^n_{x_1x_1}\big) - \frac{b}{2}\big(\eta^{n+1} + \eta^n\big) + H(R_0). \qquad (34)
\end{aligned}
$$

The discrete scheme (33)-(34) is also reported in literature as the Newmark scheme.

First we look for an energy estimate of the semi-discrete weak formulation of the momentum equation (32). In order to control the energy of the operator A we apply the Young, the trace and the Korn inequality for the individual terms from (32). After some

manipulations, cf. [28], we obtain

$$
\begin{aligned}
&||\tilde{\boldsymbol{u}}^{n+1}||^2_{L^2(\Omega^n)} + C^* \Delta t ||\tilde{\boldsymbol{u}}^{n+1}||^p_{W^{1,p}(\Omega^n)} \\
&+\rho_w \hbar \left[||\xi^{n+\frac{1}{2}}||^2_{L^2(\Gamma^0_{wall})} - ||\xi^n||^2_{L^2(\Gamma^0_{wall})} + 2\Delta t c \, ||\xi_{x_1}^{n+\frac{1}{2}}||^2_{L^2(\Gamma^0_{wall})} \right] \\
&\leq ||\boldsymbol{u}^n||^2_{L^2(\Omega^n)} + \alpha^n \Delta t ||\tilde{\boldsymbol{u}}^{n+1}||^2_{L^2(\Omega^n)} + \frac{\Delta t}{2\varepsilon} \mathrm{RHS}^{\mathrm{n+1}} + 2C^* \kappa \, \Delta t \, ,
\end{aligned} \tag{35}
$$

where $\kappa = 0$ for $p \geq 2$ and $\kappa = 1$ for $1 \leq p < 2$, $\alpha^n := ||\mathrm{div}\ \boldsymbol{w}^n||_{L^\infty(\Omega^n)}$,

$$
\begin{aligned}
\mathrm{RHS}^{\mathrm{n+1}} \ := \ & ||P_{in}(t^{n+1})||^{p'}_{L^{p'}(\Gamma_{in})} + ||P_{out}(t^{n+1})||^{p'}_{L^{p'}(\Gamma_{out})} + ||\tilde{P}_w(t^{n+1})||^{p'}_{L^{p'}(\Gamma^n_{wall})} \\
& + ||\boldsymbol{f}^{n+1}||^{p'}_{L^{p'}(\Omega^{n+1})}
\end{aligned}
$$

and C^*, C^{tr}, ε are positive constants. The dual argument $p' \geq 1$ satisfies $1/p + 1/p' = 1$.

In order to rewrite the term containing the norm $||\tilde{\boldsymbol{u}}^{n+1}||_{L^2(\Omega^n)}$ by means of $||\tilde{\boldsymbol{u}}^{n+1}||_{L^2(\Omega^{n+1})}$ and $||\boldsymbol{u}^n||_{L^2(\Omega^n)}$ we use the so-called **Geometric Conservation Law** (GCL), cf. [26, 15, 36]. It requires that a numerical scheme should reproduce a constant solution, i.e.

$$
\int_{\Omega^{n+1}} \mathrm{d}\omega^{n+1} - \int_{\Omega^n} \mathrm{d}\omega^n = \int_{t^n}^{t^{n+1}} \int_{\Omega_t} \mathrm{div}\ \boldsymbol{w} \ \mathrm{d}\omega \ \mathrm{d}t \, . \tag{36}
$$

Applying (36) to the function $|\tilde{\boldsymbol{u}}^{n+1}|^2$ we obtain

$$
||\boldsymbol{u}^{n+1}||^2_{L^2(\Omega^{n+1})} - ||\tilde{\boldsymbol{u}}^{n+1}||^2_{L^2(\Omega^n)} = \int\limits_{t^n}^{t^{n+1}} \int\limits_{\Omega_t} |\tilde{\boldsymbol{u}}|^2 \ \mathrm{div}\ \boldsymbol{w} \ \mathrm{d}\omega \ \mathrm{d}t \, . \tag{37}
$$

Taking into account the ALE-mapping, we have for $t \in (t^n, t^{n+1})$

$$
\boldsymbol{x} = \mathcal{A}_{t^n, t^{n+1}}(\boldsymbol{x}^n), \quad \mathrm{d}\omega^n = |J^{-1}_{A_{t^n, t^{n+1}}}| \ \mathrm{d}\omega \, ,
$$

where $\mathcal{A}_{t^n, t^{n+1}} := \mathcal{A}_{t^{n+1}} \circ \mathcal{A}^{-1}_{t^n}$ denotes the ALE-mapping between two time levels, J_A is the determinant of the Jacobian matrix of the ALE mapping. The right hand side of (37) can be further estimated in the following way

$$
\int\limits_{t^n}^{t^{n+1}} \int\limits_{\Omega_t} |\tilde{\boldsymbol{u}}|^2 \ \mathrm{div}\ \boldsymbol{w} \ \mathrm{d}\omega \ \mathrm{d}t \leq \beta^n \Delta t ||\boldsymbol{u}^n||^2_{L^2(\Omega^n)} \, , \tag{38}
$$

where $\beta^n := \sup\limits_{t \in (t^n, t^{n+1})} \left\{ ||\mathrm{div}\ \boldsymbol{w} \cdot |J^{-1}_{A_{t^n, t^{n+1}}}| \ ||_{L^\infty(\Omega^n)} \right\}$. Inserting (38) to (37) we obtain the desired estimate

$$
||\tilde{\boldsymbol{u}}^{n+1}||^2_{L^2(\Omega^n)} \geq ||\boldsymbol{u}^{n+1}||^2_{L^2(\Omega^{n+1})} - \beta^n \Delta t ||\boldsymbol{u}^n||^2_{L^2(\Omega^n)} \, . \tag{39}
$$

Moreover, we also obtain from (37)

$$\alpha^n \Delta t ||\tilde{\boldsymbol{u}}^{n+1}||^2_{L^2(\Omega^n)} \leq \alpha^n \Delta t ||\boldsymbol{u}^{n+1}||^2_{L^2(\Omega^{n+1})} + \alpha^n \beta^n (\Delta t)^2 ||\boldsymbol{u}^n||^2_{L^2(\Omega^n)}. \tag{40}$$

Using the inequalities (39)-(40) and summing up (35) for the first $n+1$ time steps we obtain the following estimate for the operator A

$$\begin{aligned}
&||\boldsymbol{u}^{n+1}||^2_{L^2(\Omega^{n+1})} + C^* \Delta t \sum_{i=0}^{n} ||\tilde{\boldsymbol{u}}^{i+1}||^p_{W^{1,p}(\Omega^i)} \\
&+\rho_w \hbar \sum_{i=0}^{n} \left[||\xi^{i+\frac{1}{2}}||^2_{L^2(\Gamma^0_{wall})} - ||\xi^i||^2_{L^2(\Gamma^0_{wall})} + 2\Delta t c ||\xi^{i+\frac{1}{2}}_{x_1}||^2_{L^2(\Gamma^0_{wall})} \right] \\
&\leq \left[1 + \Delta t \beta^0 + (\Delta t)^2 \alpha^0 \beta^0 \right] ||\boldsymbol{u}^0||^2_{L^2(\Omega^0)} + \Delta t \sum_{i=1}^{n+1} \left[\beta^i (1 + \alpha^i \Delta t) + \alpha^{i-1} \right] ||\boldsymbol{u}^i||^2_{L^2(\Omega^i)} \\
&+\frac{\Delta t}{2\varepsilon} \sum_{i=1}^{n+1} \mathrm{RHS}^{\mathrm{i}} + 2C^* \kappa \, T \, .
\end{aligned} \tag{41}$$

In order to estimate of the operator B we firstly multiply the equation (33) by $b(\eta^{n+1} + \eta^n)$ and the equation (34) by $(\xi^{n+1} + \xi^{n+\frac{1}{2}})$, secondly sum up the multiplied equations and then integrate them over Γ^0_{wall}. Finally, after some manipulation [28], we obtain

$$\begin{aligned}
&a||\eta^{n+1}_{x_1}||^2_{L^2(\Gamma^0_{wall})} + \frac{b}{2} \, ||\eta^{n+1}||^2_{L^2(\Gamma^0_{wall})} + ||\xi^{n+1}||^2_{L^2(\Gamma^0_{wall})} \\
&\leq a||\eta^0_{x_1}||^2_{L^2(\Gamma^0_{wall})} + \frac{3b}{2} \, ||\eta^0||^2_{L^2(\Gamma^0_{wall})} + ||\xi^0||^2_{L^2(\Gamma^0_{wall})} \\
&\quad + \sum_{i=0}^{n} \Big(||\xi^{i+\frac{1}{2}}||^2_{L^2(\Gamma^0_{wall})} - ||\xi^i||^2_{L^2(\Gamma^0_{wall})} \Big) + \frac{aL|\Gamma^0_{wall}|}{\delta}.
\end{aligned} \tag{42}$$

Here $L := \left\| \dfrac{\partial^2 R_0}{\partial x_1^2} \right\|^2_{L^\infty(\Gamma^0_{wall})}$ and δ is a small positive number.

Combining the estimates for the operator A, cf. (41), with the operator B, cf. (42), we obtain

$$E^{n+1} + \Delta t \sum_{i=1}^{n+1} G^i \leq E^0 + Q^0 + \Delta t \sum_{i=1}^{n+1} P^i + \Delta t \sum_{i=1}^{n+1} \left[\beta^i (1 + \alpha^i \Delta t) + \alpha^{i-1} \right] E^i,$$

where

$$\begin{aligned}
E^i &:= ||\boldsymbol{u}^i||^2_{L^2(\Omega^i)} + \rho_s \hbar \left[||\eta^i_{x_1}||^2_{L^2(\Gamma^0_{wall})} + \frac{b}{2} \, ||\eta^i||^2_{L^2(\Gamma^0_{wall})} + ||\xi^i||^2_{L^2(\Gamma^0_{wall})} \right] , \\
G^i &:= C^* ||\tilde{\boldsymbol{u}}^i||^p_{W^{1,p}(\Omega^{i-1})} + 2\rho_w \hbar \, c ||\xi^{i-\frac{1}{2}}_{x_1}||^2_{L^2(\Gamma^0_{wall})} , \\
Q^0 &:= \left[\Delta t \beta^0 + (\Delta t)^2 \alpha^0 \beta^0 \right] ||\boldsymbol{u}^0||^2_{L^2(\Omega^0)} + \rho_w \hbar b \, ||\eta^0||^2_{L^2(\Gamma^0_{wall})} + \frac{aL|\Gamma^0_{wall}|}{\delta} \, + 2C^* \kappa \, T, \\
P^i &:= \frac{1}{2\varepsilon} \, \mathrm{RHS}^{\mathrm{i}} ,
\end{aligned}$$

and $i = 0, \ldots, n+1$. Finally, using the discrete Gronwall lemma, cf. [42], we obtain

$$E^{n+1} + \Delta t \sum_{i=1}^{n+1} G^i \leq \left[E^0 + Q^0 + \Delta t \sum_{i=1}^{n+1} P^i \right] \exp \left\{ \sum_{i=1}^{n+1} \frac{(\beta^i(1+\alpha^i \Delta t) + \alpha^{i-1})\Delta t}{1 - (\beta^i(1+\alpha^i \Delta t) + \alpha^{i-1})\Delta t} \right\} \quad (43)$$

with the following condition on the time step

$$\Delta t \leq \frac{1}{\beta^i(1+\alpha^i \Delta t) + \alpha^{i-1}} \quad \text{for} \quad i = 0, \ldots, n+1. \quad (44)$$

We would like to point out that assuming a smooth grid movement the coefficients α^i and β^i are sufficiently small and thus the condition (44) is not very restrictive. Indeed, our estimate is more general than those obtained by Formaggia et al. [15]. The estimate (43) states that the kinetic and the dissipative energy $E^{n+1} + \Delta t \sum_{i=1}^{n+1} G^i$ is bounded with the initial and boundary data as well as a small constant arising from the smooth mesh movement.

Remark: Applying the midpoint rule for approximation of the convective ALE-term we can derive a corresponding energy estimate of the semi-discrete scheme without any dependence on the domain velocity $\boldsymbol{w}$. Here, we use the fact that in two-dimensional case the integrand on the left hand side of the geometric conservation law (37) can be exactly computed using the midpoint integration rule, cf. [26, 15, 36], i.e.

$$\int_{t^n}^{t^{n+1}} \int_{\Omega_t} |\tilde{\boldsymbol{u}}^{n+1}|^2 \operatorname{div} \boldsymbol{w} \, \mathrm{d}\omega \, \mathrm{d}t = \Delta t \int_{\Omega^{n+1/2}} |\hat{\boldsymbol{u}}^{n+1}|^2 \operatorname{div} \boldsymbol{w}^{n+1/2} \, \mathrm{d}\omega. \quad (45)$$

Here $\hat{\boldsymbol{u}}^{n+1} = \boldsymbol{u}^{n+1} \circ A_{t^{n+1}} \circ A^{-1}_{t^{n+1/2}}$ is defined on $\Omega^{n+1/2}$. As a consequence, the ALE-term will exactly balance out the integral on right hand side of (45) and the total energy at the new time step t^{n+1} will be bounded only with the initial energy and the boundary data

$$E^{n+1} + \Delta t \sum_{i=1}^{n+1} G^i \leq E^0 + \rho_w \hbar b \, ||\eta^0||^2_{L^2(\Gamma^0_{wall})} + \frac{aL|\Gamma^0_{wall}|}{\delta} + 2C^* \kappa T + \Delta t \sum_{i=1}^{n+1} P^i \, . \quad (46)$$

For more details on the derivation of energy estimates (43) and (46) the reader is referred to [28].

5 Numerical study

5.1 Hemodynamical indices

Several hemodynamical indices have been proposed in literature in order to measure the risk zones in a blood vessel. They have been introduced to describe the mechanisms correlated to intimal thickening of vessel wall. Many observations show that one reason is

the blood flow oscillations during the diastolic phase of every single heart beat. To identify the occlusion risk zones the *Oscillatory Shear Index* is usually studied in literature, see [41]

$$OSI := \frac{1}{2}\left(1 - \frac{\int_0^T \tau_w \, dt}{\int_0^T |\tau_w| \, dt}\right), \tag{47}$$

where $(0, T)$ is the time interval of a single heart beat ($T \approx 1sec$) and τ_w is the *Wall Shear Stress* (WSS) defined as

$$WSS := \tau_w = -\mathbf{T}\boldsymbol{n} \cdot \boldsymbol{\tau}. \tag{48}$$

Here $\boldsymbol{n}$ and $\boldsymbol{\tau}$ are the unit outward normal and the unit tangential vector on the arterial wall $\Gamma_{wall}(t)$, respectively. OSI index measures the temporal oscillations of the shear stress pointwisely without taking into account the shear stress behavior in an immediate neighborhood of a specific point.

It is known that the typical range of WSS in a normal artery is $[1.0, 7.0]$ Pa and in the venous system it is $[0.1, 0.6]$ Pa, see [30]. The regions of artery that are athero-prone, i.e. stimulates an atherogenic phenotype, are in the range of ± 0.4 Pa. On the other hand, the WSS greater than 1.5 Pa induces an anti-proliferative and anti-thrombotic phenotype and therefore is found to be athero-protective. In the range of $[7, 10]$ Pa high-shear thrombosis is likely to be found.

Since the viscosity of the non-Newtonian fluid is a function of shear rate, see Fig. 1, for comparison with Newtonian flow we introduce the Reynolds number for non-Newtonian models using averaged viscosity

$$Re = \frac{\rho V l}{\frac{1}{2}(\mu_0 + \mu_\infty)}, \tag{49}$$

where ρ is the fluid density, V is the characteristic velocity (e.g. maximal inflow velocity), l is the characteristic length (we take the diameter of a vessel). In order to take into account also the effects of asymptotical viscosity values, we define $Re_0 = \rho V l/\mu_0$, $Re_\infty = \rho V l/\mu_\infty$ and introduce them in the Table 1 below as well.

5.2 Computational geometry and parameter settings

We will present our numerical experiments for two test geometries. In the first one, Fig. 2 or Fig. 7, the two dimensional symmetric vessel with a smooth stenosed region is considered. Due to the symmetry we can restrict our computational domain to the upper half of the vessel. Let $\Gamma_{in} = \{(-L, x_2);\, x_2 \in (0, R(-L, t))\}$, $\Gamma_{out} = \{(L, x_2);\, x_2 \in (0, R(L, t))\}$, $\Gamma_{sym} = \{(x_1, 0);\, x_1 \in (-L, L)\}$ denote the inflow, outflow and symmetry boundary, respectively. The impermeable moving wall $\Gamma_{wall}(t)$ is modeled as a smooth stenosed constriction given as, see [31],

$$R_0(x_1) = \begin{cases} R_0(-L)\left[1 - \dfrac{g}{2}\left(1 + \cos\left(\dfrac{5\pi x_1}{2L}\right)\right)\right] & \text{if } x_1 \in [-0.4L; 0.4L] \\ R_0(-L) & \text{if } x_1 \in [-L; -0.4L) \cup (0.4L; L]. \end{cases}$$

We took $L = 5$ cm, $g = 0.3$ with $R(-L,t) = R(L,t) = 1$ cm for experiments with model data. These values give a stenosis with 30% area reduction which corresponds to a relatively mild occlusion, leading to local small increment of the Reynolds number. When considering physiological pulses prescribed by the iliac flow rate (Fig. 9, left) and the physiological viscosities (Tab. 1), the radius $R(-L,t) = R(L,t) = 0.6$ cm and the length $L = 3$ cm were chosen. This radius represents the physiological radius of an iliac artery, i.e. a daughter artery of the abdominal aorta bifurcation, cf. [46].

The bifurcation geometry shown in Fig. 8 represents the second test domain. This is a more complex geometry with asymmetric daughter vessels and the so-called sinus bulb area. Indeed, it is a simplified example of a realistic carotid artery bifurcation, see [38]. The radii of the mother vessel (i.e. common carotid artery), daughter vessels (i.e. external and internal carotid artery) and the maximal radius of the sinus bulb area are: $r_0 = 0.31$ cm, $r_1 = 0.22$ cm, $r_2 = 0.18$ cm and $r_S = 0.33$ cm. The branching angles for the bifurcation in Fig. 8 are $\gamma_1 = \gamma_2 = 25°$. We note that since the generalized string model

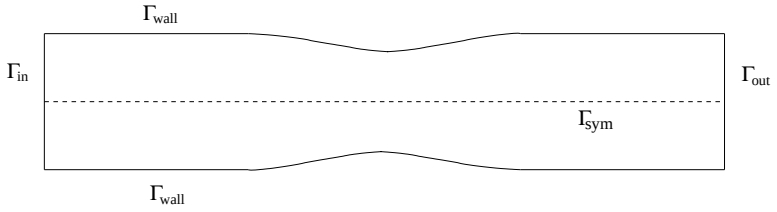

Figure 7: Stenotic reference geometry.

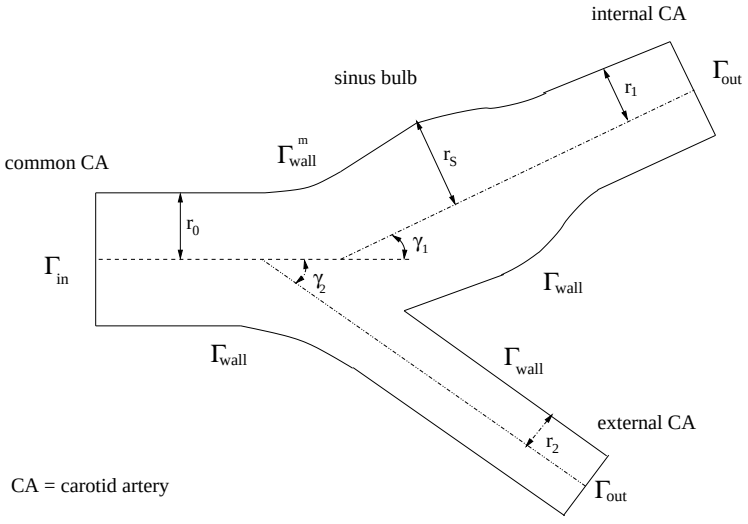

Figure 8: Bifurcation reference geometry, see [38].

has been derived for radially symmetric domains we need to preserve the radial symmetry of the geometry also after the bifurcation divider. For this purpose we rotate the original coordinate system with respect to the bifurcation angle γ_1 of the daughter vessel. In

our simulations for simplicity we assume that only one part of the boundary Γ_{wall} (this corresponds to the boundary Γ^m_{wall} in Fig. 8) is allowed to move. This is motivated by the fact that atherogenesis occurs preferably at the outer wall of daughter vessel, in particular in the carotid sinus, see [30]. Therefore this is the area of a special interest. Note that we use two different reference frames. One corresponds to the mother vessel and in the second reference frame the x_1-axis coincides with the axis of symmetry of the daughter vessel.

Boundary conditions

For Γ_{sym} the symmetry the boundary conditions $\partial_{x_2} u_1 = 0,\ u_2 = 0$ is prescribed, for Γ_{out} the Neumann type boundary condition $-\mathbf{T}\boldsymbol{n} = P_{out}\mathbf{I}\boldsymbol{n}$ is used. We prescribe the pulsatile parabolic velocity profile on the inflow boundary

$$u_1(-L, x_2) = V_{max}\frac{(R^2 - x_2^2)}{R^2} f(t), \qquad u_2(-L, x_2) = 0, \tag{50}$$

where $R = R(-L, t) = R_0(-L) + \eta(-L, t)$ and $V_{max} = u_1(-L, 0)$ is the maximal velocity at the inflow. For temporal function modeling pulses of heart $f(t)$ we have used two variants: $f(t) = sin^2(\pi t/\omega)$ with the period $\omega = 1s$, and $f(t)$ coming from physiological pulses of heart and iliac artery flow rate $Q(t)$, depicted in Fig. 9. Indeed, the flow rate is

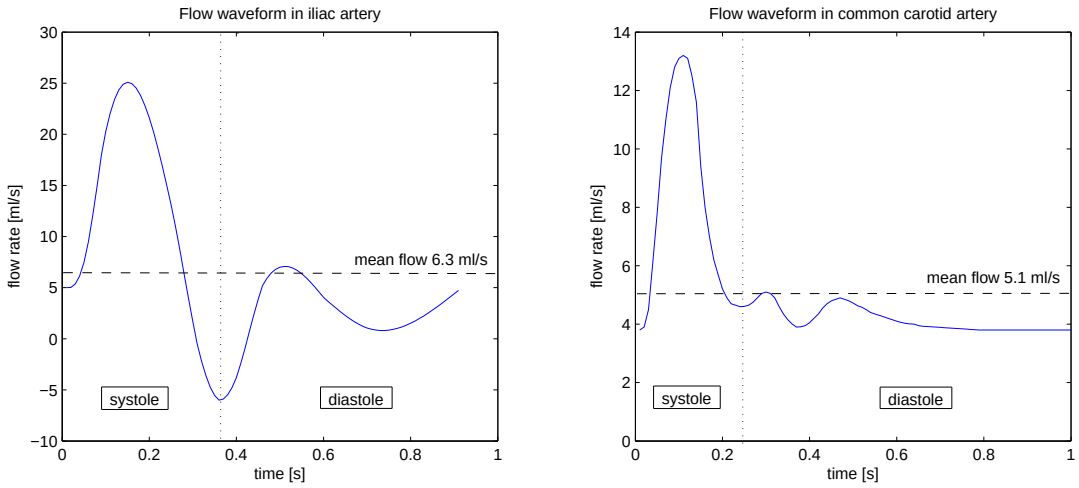

Figure 9: Flow rate $Q(t)$ in the iliac artery (left) and in a common carotid artery (right), see [38, 46].

obtained as an integral over the inflow surface S_{in}, in our case

$$Q(t) = \int_{S_{in}} u_1 dS_{in} = 2\pi \int_0^R x_2 u_1(-L, x_2) dx_2, \quad R = R(-L, t).$$

Taking into account inflow velocity (50) we obtain that $Q(t) = \frac{1}{2}\pi V_{max} R^2 f(t)$. Consequently we get the relation for temporal function $f(t)$, which we use in (50),

$$f(t) = \frac{2Q(t)}{\pi V_{max} R^2(-L,t)}. \tag{51}$$

Note that the mean inflow velocity and the maximal inflow velocity are defined by $\bar{U} = Q(t)/(\pi R^2)$ and $V_{max} = 2Q(t)/(\pi R^2)$, respectively.

Parameter settings

In the first part we have chosen in analogy to Nadau and Sequeira [31], $Re_0 = 30$ or $Re_0 = 60$ and $\mu_\infty = \frac{1}{2}\mu_0$ for the Carreau model (2) as well as for the Yeleswarapu model (3), cf. Section 5.1. For these (artificial) viscosities we will compare the hemodynamical wall parameters and study the experimental convergence of our methods. Moreover we test the stability and robustness of the method for physiological viscosity parameters [48]. The viscosity parameters for experiments with model and for physiological data are collected in Table 1 below. In order to model pulsatile flow in a vessel we use sinus pulses introduced above. In the second part we test the stability and robustness of the method

Table 1: Parameters for numerical experiments.

$Re = 34$	$Re = 80$	$Re = 40$	$Re = 80$
Carreau model $q = 0, -0.322, -0.2,\ \gamma = 1$		**Yeleswarapu model** $\gamma = 14.81$	
$\mu_\infty = 1.26P$ $\mu_0 = 2.53P$ $V_{max} = 38\,cm/s$ $Re_0 = 30$, $Re_\infty = 60$	$\mu_\infty = 0.63P$ $\mu_0 = 1.26P$ $V_{max} = 38\,cm/s$ $Re_0 = 60$, $Re_\infty = 121$	$\mu_\infty = 1.26P$ $\mu_0 = 2.53P$ $V_{max} = 38\,cm/s$ $Re_0 = 30$, $Re_\infty = 60$	$\mu_\infty = 0.63P$ $\mu_0 = 1.26P$ $V_{max} = 38\,cm/s$ $Re_0 = 60$, $Re_\infty = 121$
physiological parameters $q = -0.322,\ \gamma = 3.313$		physiological parameters	
$\mu_\infty = 0.0345P,\ \mu_0 = 0.56P$ $V_{max} = 17cm/s$ $Re = 114$, $Re_\infty = 986$		$\mu_\infty = 0.05P,\ \mu_0 = 0.736P$ $V_{max} = 22.3cm/s$ $Re = 113$, $Re_\infty = 892$	

for physiological viscosities [48] in some relevant physiological situations, e.g. in the iliac artery or in the common carotid bifurcation artery.

We note than in the human circulatory system, the Reynolds number varies significantly. Over one cycle it reaches the values from 10^{-3} up to 6000. A typical critical number for a normal artery is around 2300, for bifurcation it is around 600. However, the recirculation zones start to be created already at the Reynolds number around 170. This explains the fact that small recirculation zones appear even in healthy bifurcations. The part of a bifurcation that is the most sensitive to the local change of flow is the so-called sinus bulb area. This is a part of a daughter vessel, where an atherosclerosis is usually

formed, see Fig. 8. Indeed, our analysis of the local hemodynamical parameters confirms this fact.

In the following table we give the overview of the Reynolds numbers Re_0 and Re_∞ defined in Section 5.1 for physiological viscosities. The characteristic velocity V is taken to be the mean inflow velocity $\bar{U}$. In the Tab. 2 the Reynolds numbers for physiological pulses corresponding to the iliac artery flow rate (Fig. 9, left) and common carotid artery (Fig. 9, right) are computed. We denote by Q_{mean}, Q_{max} and Q_{min} the mean, the maximal and the minimal flow rate, respectively. The Newtonian viscosity corresponds here to μ_∞ in the Carreau model.

Table 2: Reynolds numbers for physiological data and pulses.

Iliac artery $R(0,t) = 0.6$ cm	**Newtonian model** $\mu = 0.0345P$	**Carreau model**	**Yeleswarapu model**
$Q_{mean}(t) = 6.3$ ml.s^{-1} $\bar{U} = 5.6$ cm.s^{-1}	$\mathrm{Re} \approx 195$	$\mathrm{Re}_0 \approx 12$ $\mathrm{Re}_\infty \approx 195$	$\mathrm{Re}_0 \approx 9$ $\mathrm{Re}_\infty \approx 134$
$Q_{max}(t) = 25.1$ ml.s^{-1} $\bar{U} = 22.2$ cm.s^{-1}	$\mathrm{Re} \approx 772$	$\mathrm{Re}_0 \approx 48$ $\mathrm{Re}_\infty \approx 772$	$\mathrm{Re}_0 \approx 36$ $\mathrm{Re}_\infty \approx 533$
$Q_{min}(t) = -6.0$ ml.s^{-1} $\bar{U} = -5.3$ cm.s^{-1}	$\mathrm{Re} \approx 185$	$\mathrm{Re}_0 \approx 14$ $\mathrm{Re}_\infty \approx 185$	$\mathrm{Re}_0 \approx 10$ $\mathrm{Re}_\infty \approx 114$
Carotid artery $R(0,t) = 0.31$ cm	**Newtonian model** $\mu = 0.0345P$	**Carreau model**	**Yeleswarapu model**
$Q_{mean}(t) = 5.1$ ml.s^{-1} $\bar{U} = 16.9$ cm.s^{-1}	$\mathrm{Re} \approx 304$	$\mathrm{Re}_0 \approx 19$ $\mathrm{Re}_\infty \approx 304$	$\mathrm{Re}_0 \approx 14$ $\mathrm{Re}_\infty \approx 210$
$Q_{max}(t) = 13.2$ ml.s^{-1} $\bar{U} = 43.7$ cm.s^{-1}	$\mathrm{Re} \approx 785$	$\mathrm{Re}_0 \approx 48$ $\mathrm{Re}_\infty \approx 785$	$\mathrm{Re}_0 \approx 37$ $\mathrm{Re}_\infty \approx 542$
$Q_{min}(t) = 3.9$ ml.s^{-1} $\bar{U} = 12.9$ cm.s^{-1}	$\mathrm{Re} \approx 232$	$\mathrm{Re}_0 \approx 14$ $\mathrm{Re}_\infty \approx 232$	$\mathrm{Re}_0 \approx 11$ $\mathrm{Re}_\infty \approx 160$

5.3 Discretization methods

For the numerical approximation of (1), (12) and (10) we have used as a basis the UG software package [1] and extended it for the shear-dependent fluids as well as by adding the solver for the wall deformation equation (12). In the UG package the problem class library for the Navier-Stokes equations in moving domain is based on the ALE formulation, see [3]. The Euler implicit method, the Crank-Nicolson method or the second order backward differentiation formula can be applied for time-discretization. The spatial discretization of the fluid equations (1), or (5), is realized by the finite volume method with the pseudo-compressibility stabilization. This stabilization results in the elliptic equation for the pressure. The non-linear convective term is linearized by the Newton or fixed point method, see e.g., [32]. In what follows we explain the treatment of the non-linear viscous term, which we have implemented within the UG software package.

Linearization of the viscous term

According to Taylor's expansion we have

$$\begin{aligned}\mu(\mathbf{D}(\boldsymbol{u}))\mathbf{D}(\boldsymbol{u}) &= \mu(\mathbf{D}(\boldsymbol{u}^{old}))\mathbf{D}(\boldsymbol{u}^{old}) \\ &+\frac{d\,[\mu(\mathbf{D}(\boldsymbol{u}))\mathbf{D}(\boldsymbol{u})]}{d(\nabla\boldsymbol{u})}(\boldsymbol{u}^{old})(\nabla\boldsymbol{u}-\nabla\boldsymbol{u}^{old})+\mathcal{O}((\nabla\boldsymbol{u}-\nabla\boldsymbol{u}^{old})^2),\end{aligned} \tag{52}$$

where

$$\frac{d\,[\mu(\mathbf{D}(\boldsymbol{u}))\mathbf{D}(\boldsymbol{u})]}{d(\nabla\boldsymbol{u})}(\boldsymbol{u}^{old})=\mu(\mathbf{D}(\boldsymbol{u}^{old}))\frac{1}{2}(I+I^T)+\frac{d\,\mu(\mathbf{D}(\boldsymbol{u}))}{d\nabla\boldsymbol{u}}(\boldsymbol{u}^{old})\mathbf{D}(\boldsymbol{u}^{old})$$

and $(.)^{old}$ denotes the previous iteration. Plugging the above expression for $\frac{d[\mu(\mathbf{D}(\boldsymbol{u}))\mathbf{D}(\boldsymbol{u})]}{d(\nabla\boldsymbol{u})}$ into (52) and neglecting the higher order term $\mathcal{O}((\nabla\boldsymbol{u}-\nabla\boldsymbol{u}^{old})^2)$ we obtain the Newton type iteration $\mu(\mathbf{D}(\boldsymbol{u}))\mathbf{D}(\boldsymbol{u})\approx\mu(\mathbf{D}(\boldsymbol{u}^{old}))\mathbf{D}(\boldsymbol{u})+(\nabla\boldsymbol{u}-\nabla\boldsymbol{u}^{old})\frac{d\,\mu(\mathbf{D}(\boldsymbol{u}))}{d\nabla\boldsymbol{u}}(\boldsymbol{u}^{old})\mathbf{D}(\boldsymbol{u}^{old})$. By neglecting the term $\mathcal{O}(|\nabla\boldsymbol{u}-\nabla\boldsymbol{u}^{old}|)$ we get the fixed point approximation

$$\mu(\mathbf{D}(\boldsymbol{u}))\mathbf{D}(\boldsymbol{u})\approx\mu(\mathbf{D}(\boldsymbol{u}^{old}))\mathbf{D}(\boldsymbol{u}). \tag{53}$$

We iterate with respect to $\boldsymbol{u};\boldsymbol{u}_\ell\equiv\boldsymbol{u}^{old}$, see (54). The fixed point iteration can be also understood as the Newton iteration with an incomplete Jacobian matrix, since the second part of the Jacobian matrix $\frac{d\,\mu(\mathbf{D}(\boldsymbol{u}))}{d(\nabla\boldsymbol{u})}(\boldsymbol{u}^{old})\mathbf{D}(\boldsymbol{u}^{old})$ is neglected.

Now, we present the finite volume method used in the UG package with the fixed point linearization for the viscous and convective terms and the Euler implicit time discretization

$$\begin{aligned}&\int\limits_{\Omega_i}\begin{pmatrix}(\boldsymbol{u}_{\ell+1}^{n+1}-\boldsymbol{u}^n)\\0\end{pmatrix}\,d\omega+\Delta t\int\limits_{\Omega_i}\begin{pmatrix}(\mathrm{div}\boldsymbol{w}^n)\boldsymbol{u}_{\ell+1}^{n+1}\\0\end{pmatrix}\,d\omega \\ &+\Delta t\int\limits_{\partial\Omega_i}\begin{pmatrix}[(\boldsymbol{u}_\ell^{n+1}-\boldsymbol{w}^n)\cdot\boldsymbol{n}]\boldsymbol{u}_{\ell+1}^{n+1}+[(\boldsymbol{u}_{\ell+1}^{n+1}-\boldsymbol{u}_\ell^{n+1})\cdot\boldsymbol{n}]\boldsymbol{u}_\ell^{n+1}\\0\end{pmatrix}\,dS \\ &+\Delta t\int\limits_{\partial\Omega_i}\begin{pmatrix}-(1/\rho)\mu(\mathbf{D}(\boldsymbol{u}_\ell^{n+1}))(\bigtriangledown\boldsymbol{u}_{\ell+1}^{n+1}\cdot\boldsymbol{n})+(1/\rho)p_{\ell+1}^{n+1}\,(\mathbf{I}\cdot\boldsymbol{n})\\ \boldsymbol{u}_{\ell+1}^{n+1}\cdot\boldsymbol{n}-h^2\bigtriangledown(p_{\ell+1}^{n+1}-p_\ell^{n+1})\cdot\boldsymbol{n}\end{pmatrix}\,dS=0.\end{aligned} \tag{54}$$

In the case of the global iterative method Ω_i denotes the i-th control volume at time t^{n+1} given from the previous iteration, i.e. $\Omega_i=\Omega_i^{(k-1)}(t^{n+1})$. The grid velocity $\boldsymbol{w}^n=\boldsymbol{w}(t^n)$ is obtained using the backward difference of the grid position $\boldsymbol{w}^n=\frac{\boldsymbol{x}^{n+1,\,(k-1)}-\boldsymbol{x}^n}{\Delta t}$. In the case of the kinematical splitting we have $\Omega_i=\Omega_i(t^n)$ and $\boldsymbol{w}^n=\frac{\boldsymbol{x}^n-\boldsymbol{x}^{n-1}}{\Delta t}$.

Discretization of structure equation

In order to approximate the structure equation we apply the finite difference method. For the global iterative method we will rewrite the second order equation (12) as a system of

two first order equations. Set $\xi = \partial_t \eta$. Time discretization is realized by the following scheme

$$\begin{aligned} \frac{\xi^{n+1}-\xi^n}{\Delta t} - a\alpha\frac{\partial^2\eta^{n+1}}{\partial x_1^2} &+ b\alpha\eta^{n+1} - c\alpha\frac{\partial^2\xi^{n+1}}{\partial x_1^2} \\ &= H + a(1-\alpha)\frac{\partial^2\eta^n}{\partial x_1^2} - b(1-\alpha)\eta^n + c(1-\alpha)\frac{\partial^2\xi^n}{\partial x_1^2} \\ \frac{\eta^{n+1}-\eta^n}{\Delta t} &= \alpha\xi^{n+1} + (1-\alpha)\xi^n, \end{aligned} \tag{55}$$

where

$$a = \frac{|\sigma_{x_1}|}{\rho_w}\left[1+\left(\frac{\partial R_0}{\partial x_1}\right)^2\right]^{-2}, \quad b = \frac{E}{\rho_w R_0(R_0+\eta)} + \frac{(\tilde{\mathbf{T}} + \tilde{P_w}\mathbf{I})\cdot\tilde{\boldsymbol{n}}\cdot\boldsymbol{e}_r}{R_0\rho_w\hbar},$$

$$c = \frac{\gamma}{\rho_w\hbar}, \quad H = H(\boldsymbol{u},p) + H(R_0) = -\frac{(\tilde{\mathbf{T}} + \tilde{P_w}\mathbf{I})\cdot\tilde{\boldsymbol{n}}\cdot\boldsymbol{e}_r}{\rho_w\hbar} + a\frac{\partial^2 R_0}{\partial x_1^2}\ .$$

We note that in contrary to the definitions given by (27) and (31), we included a part of the right hand side term having the factor η/R_0 to the coefficient b. Moreover, due to the linear elasticity assumption we assumed small deformation gradient $\partial\eta/\partial x_1$, which yields $\frac{\sqrt{1+\left(\partial_{x_1}(R_0+\eta)\right)^2}}{\sqrt{1+\left(\partial_{x_1}R_0\right)^2}} \approx 1$.

Constants appearing in the coefficients a, b, c have typically following values, see [14]: the Young modulus is $E = 0.75\times10^5 dyn.cm^{-2}$, the wall thickness $\hbar = 0.1\ cm$, the density of the vessel wall tissue $\rho_w = 1.1\ g.cm^{-3}$, the viscoelasticity constant $\gamma = 2\times10^4\ P.s.cm^{-1}$, $|\sigma_z| = G\kappa$, where $\kappa = 1$ is the Timoshenko shear correction factor and G is the shear modulus, $G = E/2(1+\sigma)$, where $\sigma = 1/2$ for incompressible materials.

If $\alpha = 0$ we have an explicit scheme in time, for $\alpha = 1$ we obtain an implicit scheme. The parameter $\alpha = \frac{1}{2}$ yields the Newmark scheme, which is proven to be unconditionally stable at least in the case of homogeneous Dirichlet boundary conditions, see [36].

In the case of kinematical splitting algorithm, the structure equation (26) is discretized using the splitting approach (29)-(30). The operator A consists of (54) and (56), where

$$\frac{\xi^{n+1/2}-\xi^n}{\Delta t} = c\alpha\ \xi^{n+1/2}_{x_1x_1} + c(1-\alpha)\ \xi^n_{x_1x_1} + H(p^{n+1},\boldsymbol{u}^{n+1}). \tag{56}$$

The parameter α is chosen to be either 0.5 or 1. A new solution obtained from (54), (56) is the velocity $\tilde{\boldsymbol{u}}^{n+1}$ and the pressure $\tilde{p}^{n+1}$ on Ω^n as well as the wall velocity function $\xi^{n+1/2}$ on Γ^n_{wall}. The second step is the operator B, that combines the purely elastic part of structure equation and the kinematical coupling condition (28). This can be discretized in an explicit or implicit way. An explicit scheme reads as follows

$$\begin{aligned} \frac{\eta^{n+1}-\eta^n}{\Delta t} &= \alpha_1\ \xi^{n+1/2} + (1-\alpha_1)\ \xi^n, \\ \frac{\xi^{n+1}-\xi^{n+1/2}}{\Delta t} &= a\alpha_2\ \eta^{n+1}_{x_1x_1} + a(1-\alpha_2)\ \eta^n_{x_1x_1} - b\alpha_2\ \eta^{n+1} - b(1-\alpha_2)\ \eta^n + H(R_0) \end{aligned} \tag{57}$$

for $\alpha_1 = 0.5,\ \alpha_2 \in \{0.5; 1\}$. An implicit scheme has the following form

$$\begin{aligned} \frac{\eta^{n+1} - \eta^n}{\Delta t} &= \alpha_1\ \xi^{n+1} + (1-\alpha_1)\ \xi^{n+1/2} \\ \frac{\xi^{n+1} - \xi^{n+1/2}}{\Delta t} &= a\alpha_2\ \eta^{n+1}_{x_1x_1} + a(1-\alpha_2)\ \eta^{n}_{x_1x_1} - b\alpha_2\ \eta^{n+1} - b(1-\alpha_2)\ \eta^n + H(R_0) \end{aligned} \tag{58}$$

for $\alpha_1 = 0.5,\ \alpha_2 = 0.5$. We note that once new values for the wall displacement η^{n+1} and the velocity ξ^{n+1} are known, we update the fluid velocity on the moving boundary to $\boldsymbol{u}^{n+1}$ and update the mesh. In our experiments we have used both, the explicit (57) as well as the implicit method (58). The implicit coupling was typically more stable. In order to combine the operators A and B we may use the first order **Marchuk-Yanenko operator splitting** or the second order **Strang splitting** scheme. The Marchuk-Yanenko scheme

$$\mathcal{U}^{n+1} = B_{\triangle t} A_{\triangle t}\, \mathcal{U}^n,$$

where $\mathcal{U}^n$ is the approximate solution of the coupled fluid-structure interaction problem at the time level t^n. The second order Strang splitting yields

$$\mathcal{U}^{n+1} = B_{\triangle t/2} A_{\triangle t} B_{\triangle t/2}\, \mathcal{U}^n.$$

5.4 Numerical experiments

We start with the comparison of our two fluid-structure interaction schemes: the global iterative method and the kinematical splitting. In Fig. 10 we can see the domain deformation at two different time steps, that was obtained using the global iterative method, cf. (55) with $\alpha = \frac{1}{2}$ (Newmark scheme) and the explicit kinematical splitting (56), (57) with $\alpha = \alpha_1 = \alpha_2 = \frac{1}{2}$. We can see that both methods yield analogous results.

Our next aim is to investigate differences in the behavior of Newtonian and non-Newtonian fluids in moving domains for different viscosity data and Reynolds numbers. Experiments presented in Section 5.4.1 as well as in the first part of Section 5.4.2 were obtained using the global iterative method. In Section 5.4.2 experiments using the kinematical splitting method for the iliac artery and the carotid bifurcation will be presented.

5.4.1 Numerical experiments for model data

In this subsection we present experiments with the viscosity parameters introduced in the first three lines of Table 1 for model data. The Reynolds number for non-Newtonian fluids varies between two values Re_0 and Re_∞. In order to compare similar flow regimes, the same Reynolds number $Re = 40$ for the Newtonian as well as the non-Newtonian fluids was used. The corresponding Newtonian viscosity was chosen such that it coincides with the averaged non-Newtonian viscosity $\frac{1}{2}(\mu_0 + \mu_\infty)$, see (49).

We use the Dirichlet inflow boundary condition (50), which models pulsatile parabolic velocity profile at the inflow. Here we took $f(t) = sin^2\,(\pi t/\omega)$ with $\omega = 1s$. We have

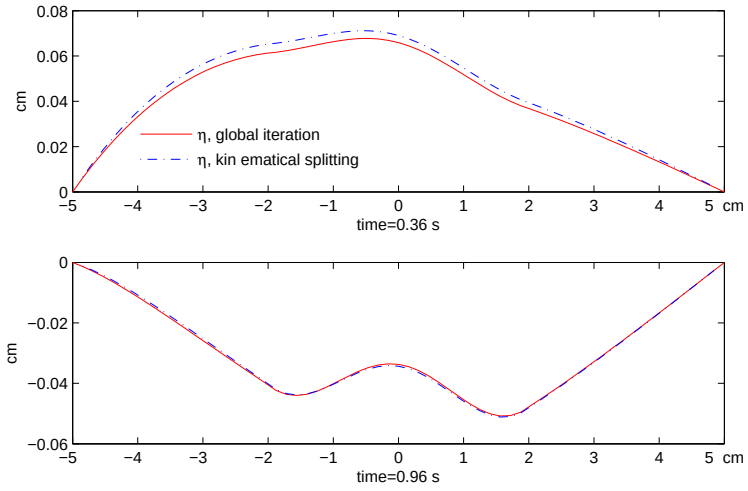

Figure 10: Comparison of the wall deformation η in a stenosed vessel for the global iterative method and the explicit kinematical splitting, Re=40.

chosen two non-Newtonian models for the blood flow often used in the literature, the Carreau and the Yeleswarapu model. Further, we study the influence of non-Newtonian rheology and of fluid-structure interaction on some hemodynamical wall parameters such as the wall shear stress WSS and the oscillatory shear index OSI. In what follows we plot the results comparing several aspects of Newtonian and non-Newtonian flow in the straight channel and in the channel with a stenotic occlusion.

Fig. 11 describes time evolution of the wall deformation function η at two time instances $t = 0.36s$ and $t = 0.96s$ for the straight and stenotic compliant vessel and for different non-Newtonian viscosities. Clearly, we can see effects due to the presence of stenosis in Fig. 11. The differences in wall deformation for non-Newtonian and Newtonian fluids are not significant.

Fig. 12, 13 describe the wall shear stress distribution WSS along the moving or fixed (solid) wall in the straight and in stenotic vessel, respectively. We compare the WSS for the Newtonian and non-Newtonian fluids. Analogously as before we see that the WSS depends considerably on the geometry. In Fig. 13 peaks in the WSS due to the stenosis can be identified clearly for both Newtonian and non-Newtonian models. Fluid rheology is even more significant for WSS measurements; see different behaviour of WSS at $t = 0.36s$ in Fig. 12 and Fig. 13. Moreover, we can conclude that the WSS at $t = 0.36s$ is in general lower in a compliant vessel than in a solid one, see Fig. 12 for the straight and Fig. 13 for the stenotic vessel.

Another important hemodynamical wall parameter is the oscillatory shear index OSI. Fig. 14 describes the behavior of the OSI in the straight and stenotic vessel (both solid and compliant case). We can see new effects due to the presence of stenosis in the OSI. Moreover the peaks in the OSI are more dominant for the non-Newtonian models in

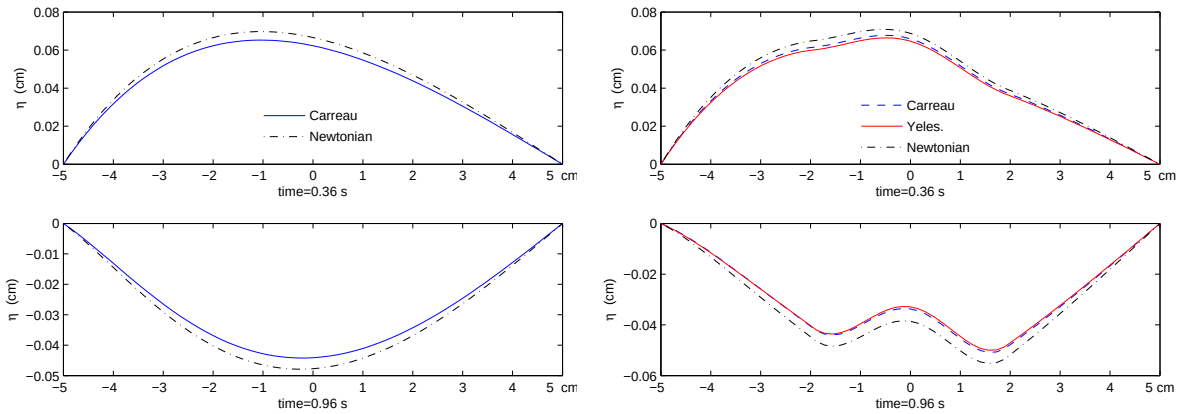

Figure 11: Deformation of the compliant wall η, left: a straight vessel, right: a stenosed vessel, $Re = 40$.

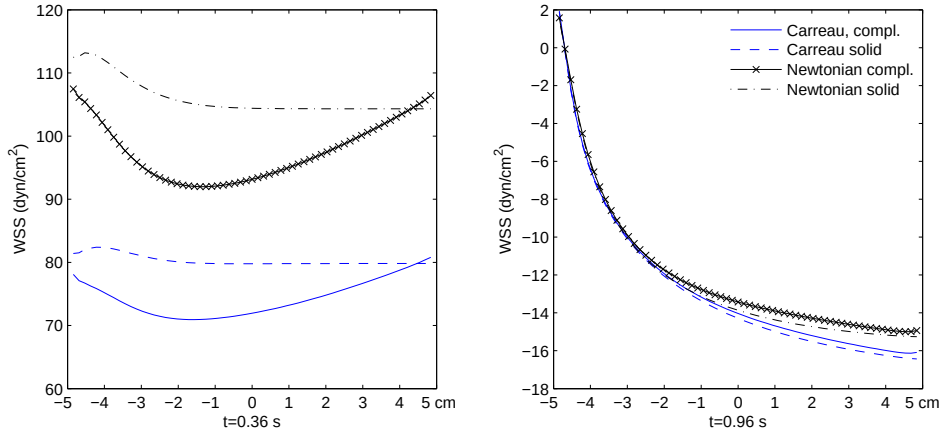

Figure 12: WSS along the straight vessel with solid as well as compliant walls, the Newtonian and the Carreau model, $Re = 40$, left: $t = 0.36s$, right: $t = 0.96s$.

comparison to the Newtonian flow. High OSI values indicate the areas with the large stenotic plug danger. Fig. 14 indicates, that such areas appear at the end of stenotic reduction. Numerical simulation with solid vessel walls indicates even higher oscillation of the wall shear stress. Thus, simulations without fluid-structure interaction would indicate more critical shear stress situation in vessels as they are actually present in elastic moving vessels.

We conclude this subsection with a statement, that the fluid rheology and domain geometry may have a considerable influence on the hemodynamical wall parameters WSS and OSI. The fluid-structure interaction aspect plays definitely significant role in the prediction of hemodynamical indices and should be involved in reliable computer simulations.

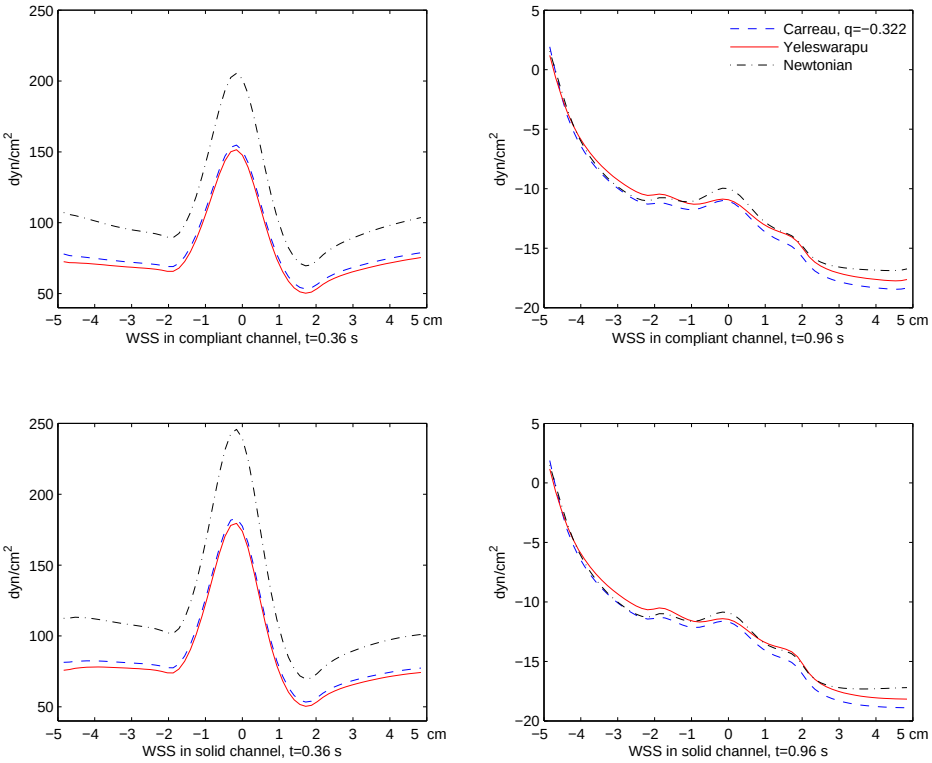

Figure 13: WSS along the vessel wall in a stenosed compliant (top) and solid (bottom) vessel at two time instances, $Re = 40$.

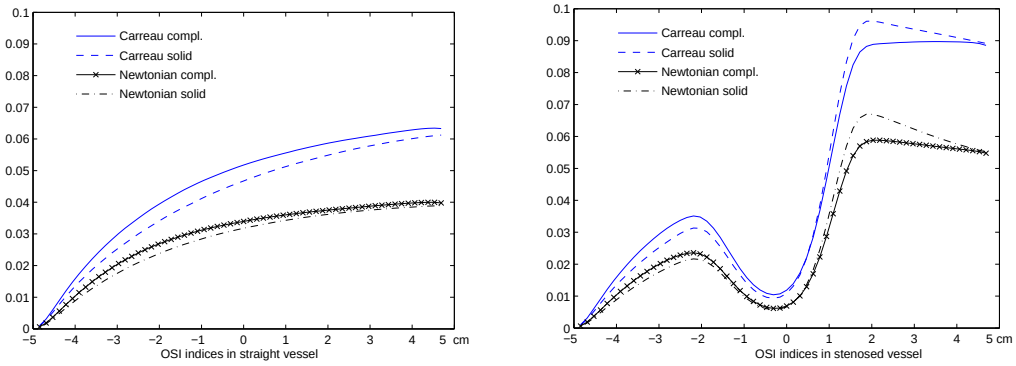

Figure 14: OSI indices along the compliant and the solid vessel wall, the straight vessel (left) and the stenosed vessel (right), $Re = 40$.

5.4.2 Numerical experiments for physiological data

Several results comparing the behavior of both non-Newtonian models, the Carreau and the Yeleswarapu model with corresponding physiological viscosities from Table 1, cf. lines

4 and 5, are presented below. We consider here pulsatile velocity profile at the inflow as in Section 5.4.1 and zero Dirichlet boundary conditions for η.

Fig. 15 describes the velocity field, streamlines and the pressure distribution at two time instances. We can clearly notice reversal flow areas due to pulsatile behavior of blood flow. At time $t = 0.96$ s, where the inflow velocity is decreasing, we can observe vortices in the streamlines. In what follows we compare measurements for increasing Reynolds

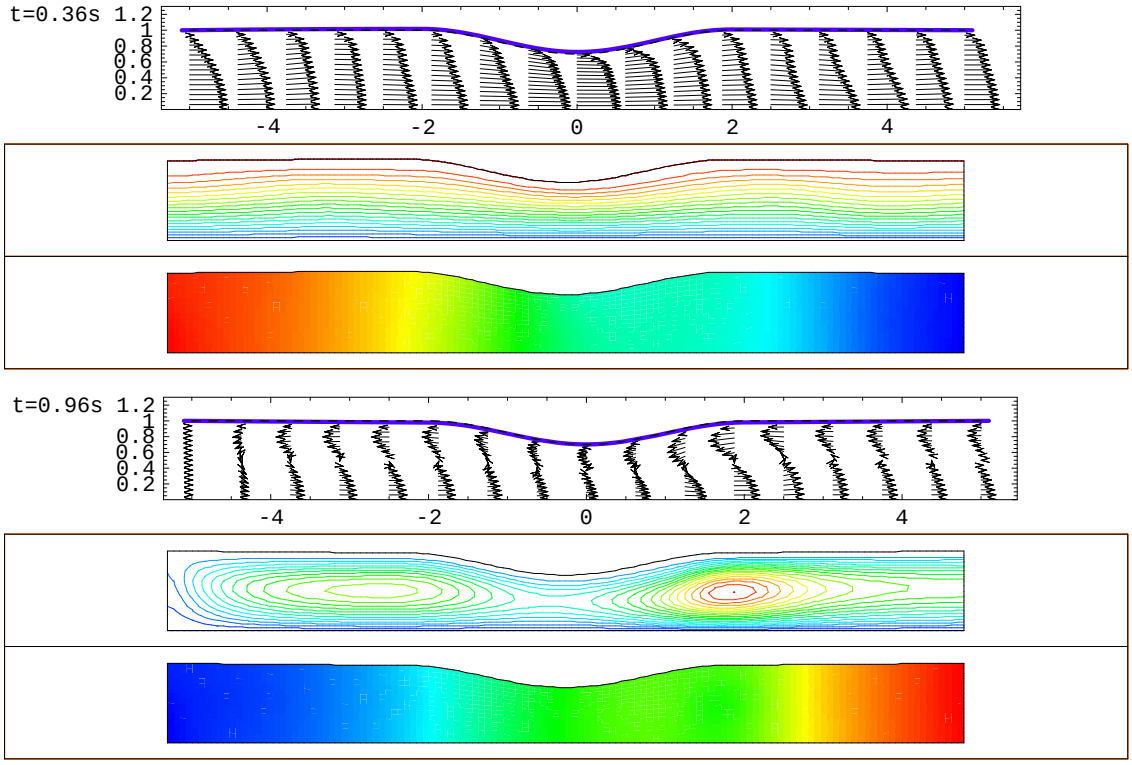

Figure 15: Numerical experiment using physiological parameters: the Carreau model, $t = 0.36s$ (top) and $t = 0.96s$ (bottom), from above: velocity field, streamlines and pressure distribution.

numbers, namely for $Re = 114$ and $Re = 182$. For comparison with the Newtonian case, we are using two values of the corresponding Newtonian viscosity. One Newtonian viscosity, similarly as in the previous Section 5.4.1, is obtained from the averaged non-Newtonian viscosity $\mu = \frac{1}{2}(\mu_0 + \mu_\infty)$. The second one is the physiological viscosity $\mu = 0.0345\ P$.

Our numerical experiments confirm, that the differences between Newtonian (both physiological and averaged viscosity) and non-Newtonian fluids in the wall deformation, the wall shear stress WSS as well as in the oscillatory shear index OSI are more dominant with increasing Reynolds numbers, see Figs. 16, 17, 18. We can also observe that the amplitude of wall displacement and wall shear stress is smaller for the physiological Newtonian velocity and larger for the averaged Newtonian velocity. This means that concerning

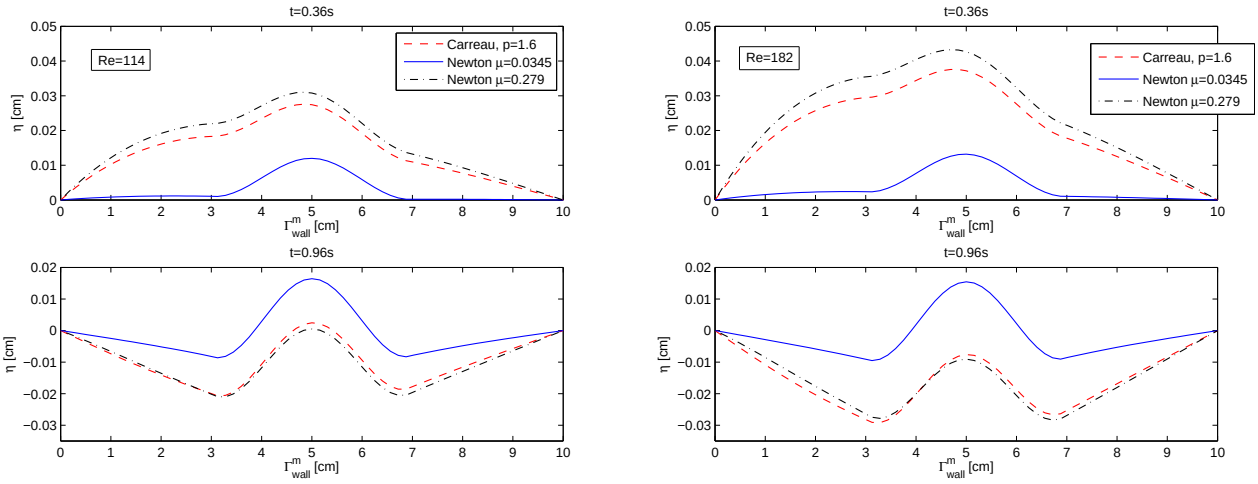

Figure 16: Comparison of wall deformations for different Reynolds numbers, left: Re=114, right: Re=182, at two time instances $t = 0.36s$, $t = 0.96s$.

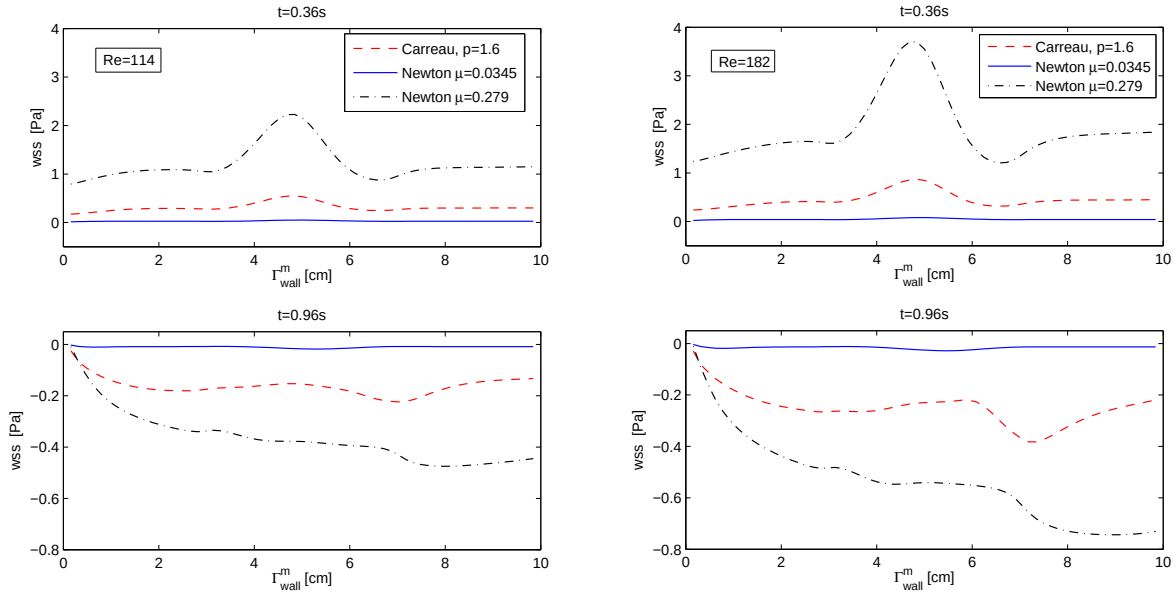

Figure 17: Comparison of wall shear stresses WSS for different Reynolds numbers, left: Re=114, right: Re=182, at two time instances $t = 0.36s$, $t = 0.96s$.

physiological Newtonian viscosity (or averaged Newtonian viscosity) the hemodynamical parameters predict more (or less) critical situation in the case of Newtonian flow than by the non-Newtonian flow.

Concerning the oscillatory shear index OSI, see Fig. 18, the higher Reynolds number corresponds to the higher values of OSI. It shows that increasing the Reynolds number,

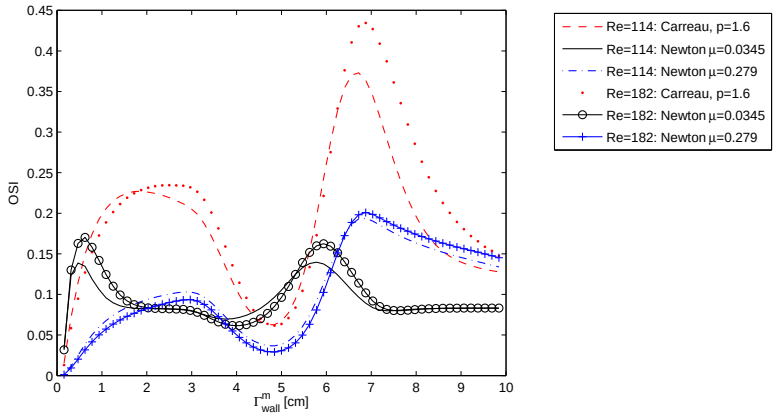

Figure 18: OSI indices for different Reynolds numbers using physiological viscosities.

the amplitude of WSS increases and the period of reversed flow prolongates.

Iliac artery and carotid bifurcation

In this part we present experiments for physiological situations, including a simplified but realistic geometry (Figs. 7,8), physiological flow rate (Fig. 9) as well as the physiological viscosities (Newtonian viscosity $\mu = 0.0345$ P and non-Newtonian viscosities from Tab. 1).

Figs. 19, 20 (left) demonstrate dependence of the wall displacement on the reference geometry. From the evolution of the wall movement for several time instances corresponding to systolic maximum, systolic minimum, diastolic minimum and the final phase of the physiological flow for the Carreau viscosity we conclude that the presence of stenosis as well as bifurcation divider influences the compliance of the vessel wall. Comparing the Newtonian as well as non-Newtonian rheology (Figs. 19, 20, right) we see that the difference between them is not significant.

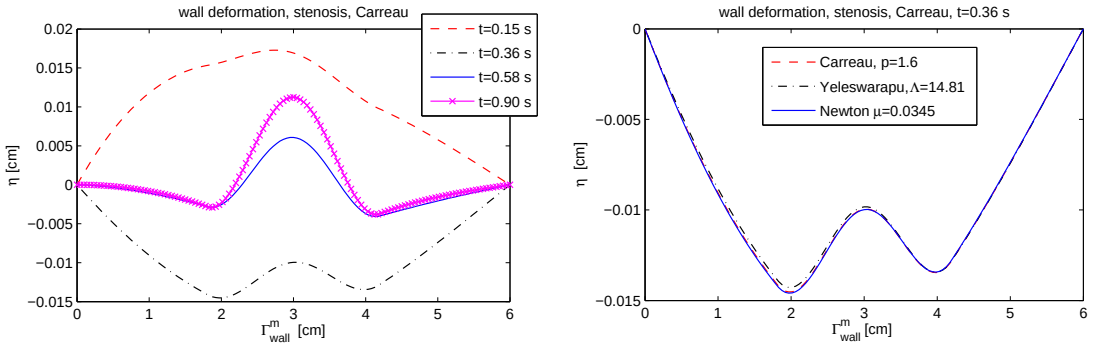

Figure 19: The evolution of η along the line $x_2 = R_0$ for stenosed vessel. Left: comparison at several time instances, right: comparison of different constitutive models at $t = 0.36$ s.

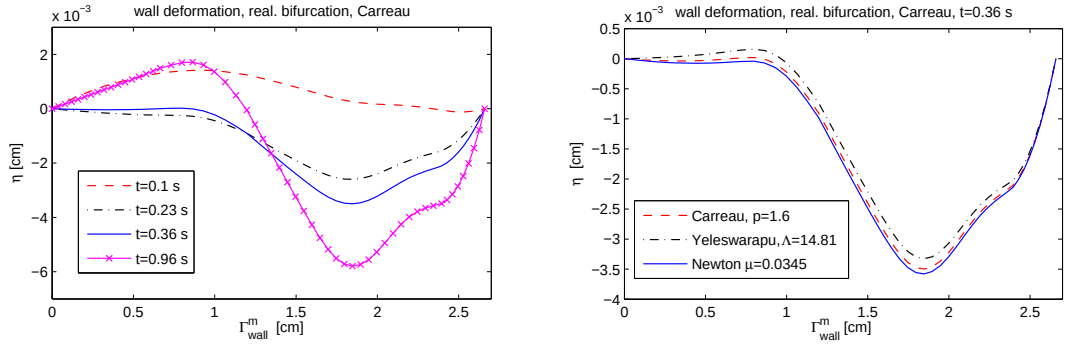

Figure 20: The evolution of η along the moving boundary Γ^m_{wall} for bifurcation geometry. Left: comparison at different time instances, right: comparison of constitutive models at $t = 0.36$ s.

The WSS distribution along the moving boundary for both types of geometry is presented in Figs. 21, 22. We see that the peak of the WSS corresponds to the stenosed area (see Fig. 21) and to the bifurcation divider (see Fig. 22). In the case of stenosed vessel we

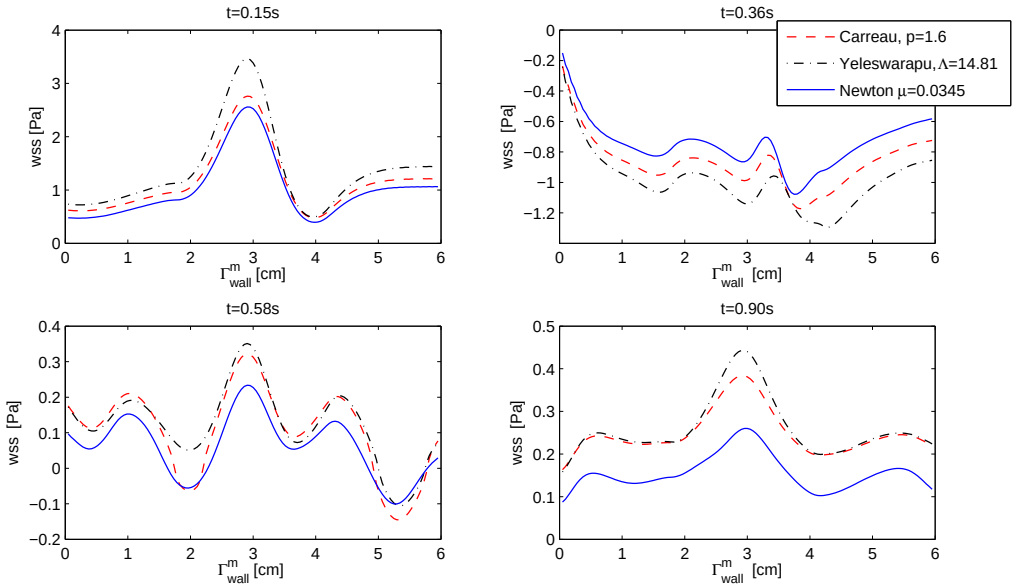

Figure 21: WSS along Γ_{wall} for the stenotic vessel geometry at several time instances.

observe one reversed vortex at $t = 0.36$ s and two vortices at $t = 0.58$ s. Moreover, at time instances $t = 0.58$ s and $t = 0.90$ s, the WSS belongs to the athero-prone range. Looking at the bifurcation geometry (Fig. 22), a reversed flow at all time instances around the sinus bulb appears. Moreover, approaching the bifurcation divider lower values of the WSS can be found. In both cases, stenotic iliac and bifurcation carotid artery, we observe that the WSS corresponding to the non-Newtonian model gives higher extremal values.

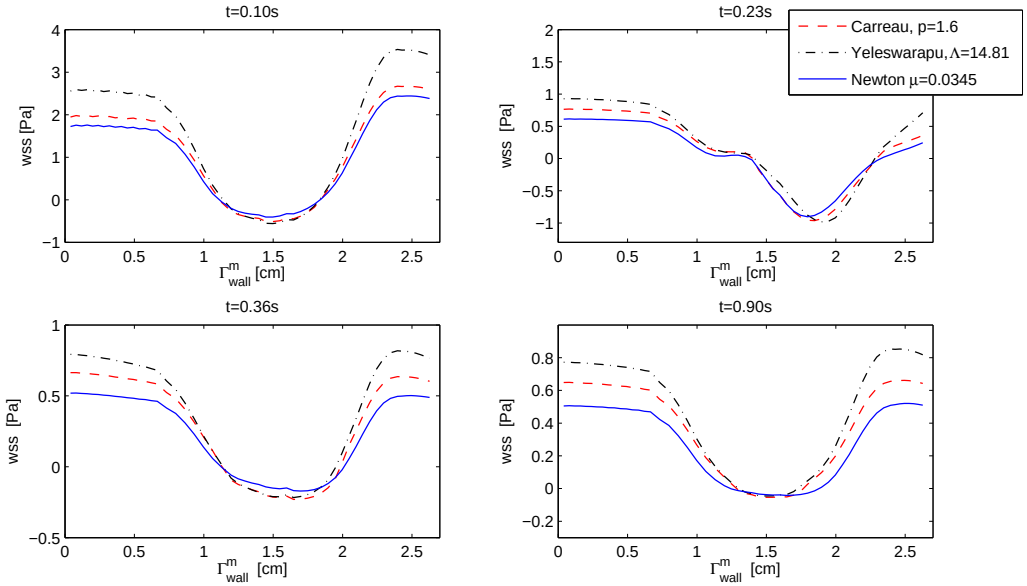

Figure 22: WSS along Γ^m_{wall} for the bifurcation geometry at several time instances.

In Fig. 23 the OSI index along the moving boundary for stenotic (left) and bifurcation geometry (right) is presented. Due to the high shear flow in a stenosed region, direction-varying WSS, in particular before and after stenosis, can be found. In the case of carotid bifurcation, the OSI peak corresponds to the sinus bulb area. These measurements agree with the observations from the clinical praxis, e.g. [30].

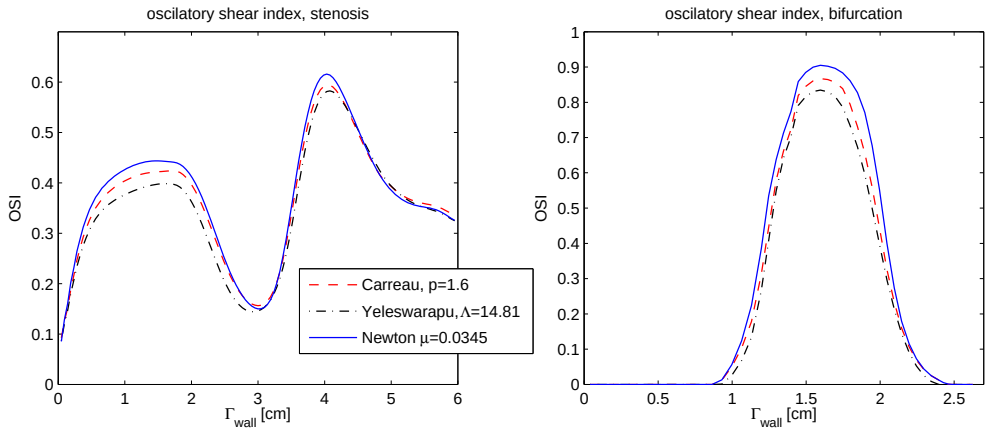

Figure 23: OSI along Γ_{wall}. Left: stenosed geometry, right: bifurcation geometry.

a) $t = 0.27$ s

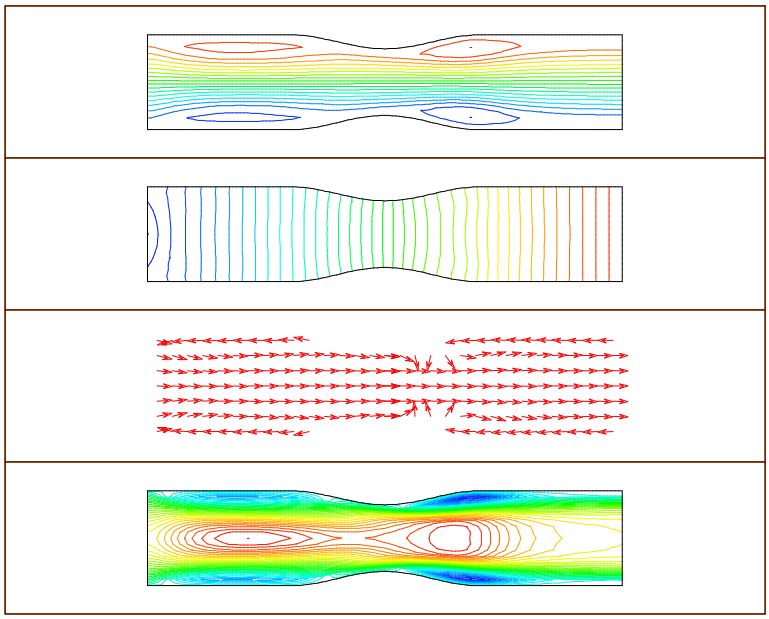

b) $t = 0.36$ s

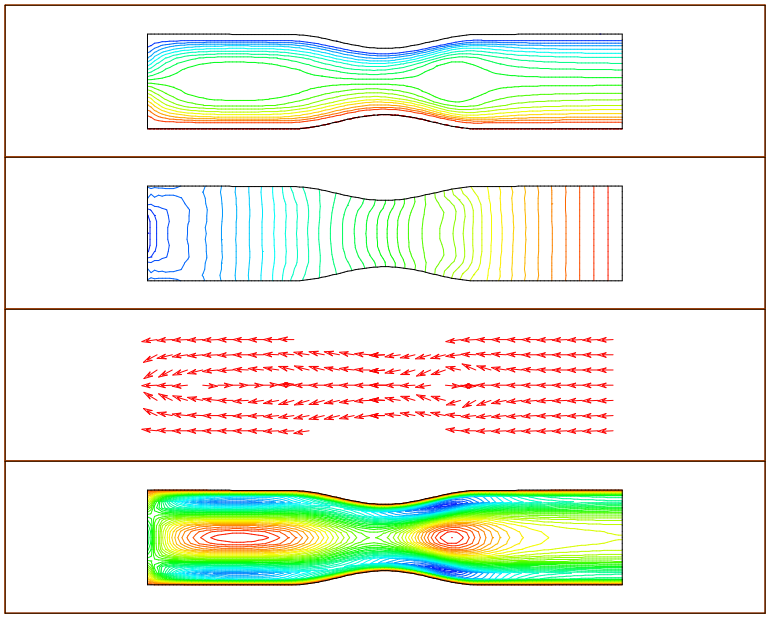

Figure 24: Velocity streamlines, pressure isolines, velocity vector field and horizontal velocity isolines for the stenosed vessel at two time instances.

a) $t = 0.23$ s

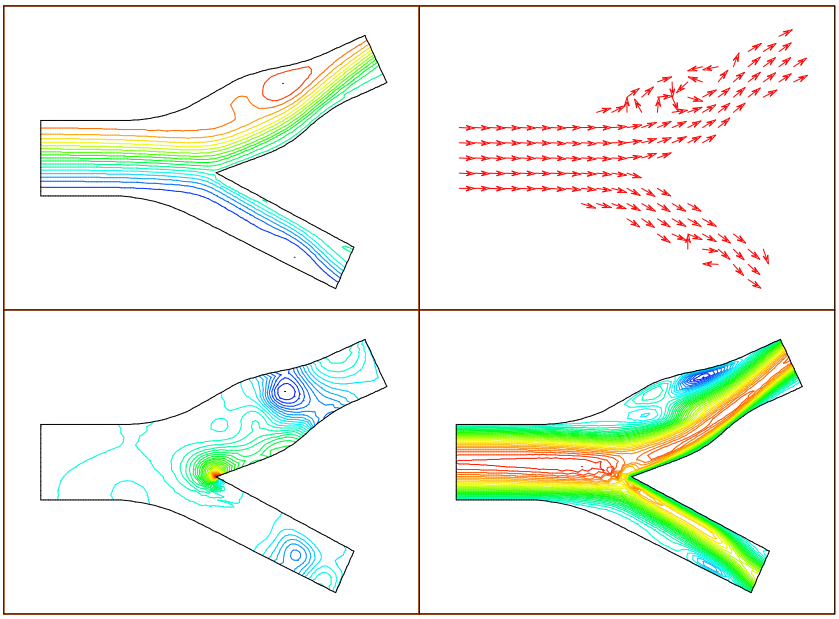

b) $t = 0.36$ s

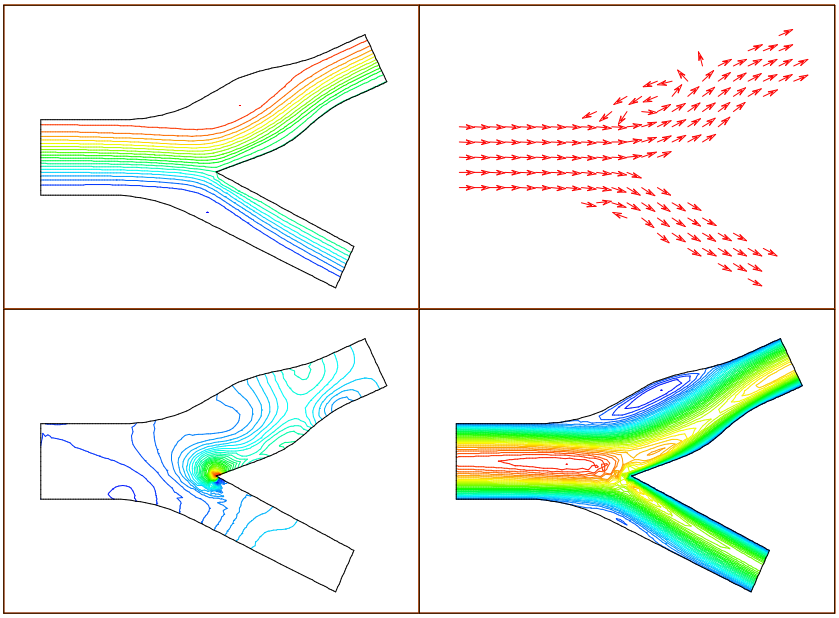

Figure 25: Velocity streamlines, velocity vector field, pressure isolines and horizontal velocity isolines for the bifurcation geometry at two time instances.

Finally, Figs. 24, 25 present several snapshots for the stenotic and bifurcation geometry depicting the velocity streamlines, velocity vector field, pressure isolines and horizontal velocity isolines. In Fig. 24a we observe the development of recirculation zones around the stenosed area. At the systolic minimum (Fig. 24b) we can see that the negative flow with pressures from $[-51.6, 0]$ Pa and horizontal velocities from $[-21.5, 7.8]$ cm.s^{-1} develops. In the case of bifurcation geometry, we observe the development of reversed flow in particular in the sinus bulb area (Fig. 25). We note that due to the bifurcation geometry the axial velocity profiles in daughter vessels are asymmetric. For more details on physiological experiments, including the evolution of WSS for chosen points on moving boundary, see [28].

5.5 Convergence study

In our numerical experiments we have used piecewise linear approximations for fluid velocities and for pressure and backward Euler method for time discretization. In the case of global iterative method the structure equation is approximated by the second order Newmark method. For the kinematical splitting method the second order approximation in space and time (Crank-Nicolson method) was applied. Both the first order Marchuk-Yanenko splitting as well as the second order Strang splitting schemes have been tested.

In order to study accuracy of the coupled fluid-structure interaction problem the so-called **experimental order of convergence** (EOC) is computed. The EOC in space is defined in the following way

$$EOC(\boldsymbol{u}) = \log_2 \frac{\|\boldsymbol{u}_{h,\Delta t} - \boldsymbol{u}_{\frac{h}{2},\Delta t}\|_{L^p} / \|\Omega_h\|_{L^p}}{\|\boldsymbol{u}_{\frac{h}{2},\Delta t} - \boldsymbol{u}_{\frac{h}{4},\Delta t}\|_{L^p} / \|\Omega_{\frac{h}{2}}\|_{L^p}} \,. \tag{59}$$

To evaluate the EOC in space, the computational domain $\Omega(\eta)$ is consecutively divided into 16×2 elements (1. refinement), 32×4 elements (2. refinement), 64×8 elements (3. refinement), 128×16 elements (4. refinement), where the element size $h = (\Delta x, \Delta y)$ is halved. The space errors and the EOC were computed at $T = 0.8s$. The constant time step was chosen to be enough small and set to $\Delta t = 0.002s$.

We consider here the Carreau model for non-Newtonian fluid as well as the Newtonian fluid. The index p denotes the corresponding exponent in the power-law model used for the non-Newtonian Carreau viscosity function, see (2). In our case we took $q = -0.2$, which yields $p = 1.6$ as well as $q = 0$ ($p = 2$) in the Newtonian case. Note that due to the regularity results presented in Subsection 4.1.1 we measure the errors in the L^p, or $W^{1,p}$, norm for velocity for the non-Newtonian fluid and in the L^2, or $W^{1,2}$, norm for the Newtonian fluid. Due to the artificial compressibility regularization of the continuity equation we can measure pressure in the L^2 norm.

Let us firstly present the convergence results in space in term of the EOC values for velocity and pressure in a rigid domain, Tab. 3. For each quantity a following notation for the normalized L^p-error was used

$$Err(\boldsymbol{u}) = \frac{\|\boldsymbol{u}_{h,\Delta t} - \boldsymbol{u}_{h/2,\Delta t}\|_{L^p}}{\|\Omega_h\|_{L^p}}.$$

Table 3 presents convergence results in a fixed domain with the symmetry boundary

Table 3: Convergence rates in space, rigid domain.

	Newtonian fluid				Carreau fluid, $q = -0.2$			
# of refin.	$Err(\boldsymbol{u})$	EOC	$Err(p)$	EOC	$Err(\boldsymbol{u})$	EOC	$Err(p)$	EOC
	L^2 norm				L^p norm		L^2 norm	
2/1	1.0783		3.5199		0.9083		3.7209	
3/2	0.2758	1.967	0.6870	2.357	0.2494	1.865	0.7073	2.395
4/3	0.084	1.715	0.3204	1.101	0.1092	1.192	0.1577	2.165

conditions at the central line, see Fig. 26. We can notice slightly worse than second order convergence rate in velocity for the Newtonian case. Moreover, in the non-Newtonian case the convergence in velocity is reduced to 1. This effect can be explained by the influence of symmetry boundary conditions coupled with the Neumann boundary conditions. On the other hand this boundary conditions improve convergence of pressure in the non-Newtonian case to the second order.

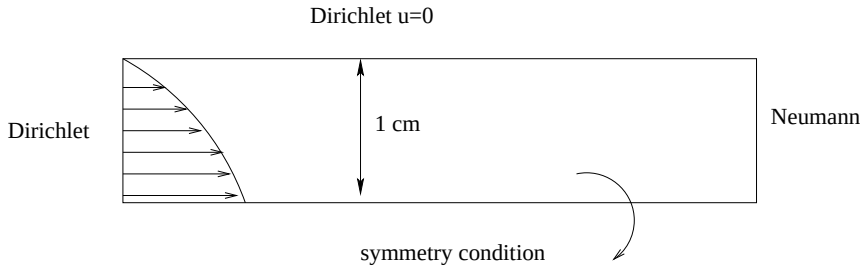

Figure 26: Boundary conditions in measurements of EOC .

In the next experiment we compare the order of convergence of the kinematical splitting algorithm, see Tab. 5 and the global iterative method, see Tab. 4. We can clearly see

Table 4: Convergence rates in space: global iterative method, the Carreau model.

# of refin.	$Err\ (\boldsymbol{u})$	EOC	$Err\ (\eta)$	EOC	$Err\ (p)$	EOC
	L^p-norm		L^2-norm			
2/1	0.9512		2.81 e-3		3.3925	
3/2	0.2563	1.89	8.88 e-4	1.69	0.7113	2.25
4/3	0.1074	1.26	1.85 e-4	2.23	0.1577	2.17

the similar convergence rates in velocities, pressures and displacements that are higher than first order for velocities and the second order for pressures and wall displacements. We also observe decreasing convergence rate for velocity for finer meshes, which was also

Table 5: Convergence rates in space: kinematical splitting (Marchuk-Yanenko), the Carreau model.

# of refin	$Err\,(\boldsymbol{u})$	EOC	$Err(\nabla\boldsymbol{u})$	EOC	$Err\,(\eta)$	EOC	$Err\,(p)$	EOC
	L^p-norm				L^2-norm			
2/1	0.8971		0.9682		2.62 e-4		3.1338	
3/2	0.2466	1.86	0.1408	2.78	1.84 e-5	0.51	0.7026	2.16
4/3	0.1051	1.23	0.0435	1.69	0.38 e-5	2.26	0.1461	2.27

observed in the rigid domain, Table 3, and may be caused by the boundary conditions. Let us point out that the kinematical splitting approach yields 10 times smaller relative errors in the wall displacement than the strong coupling scheme. This weak coupling method is also more efficient as the global iterations with respect to the domain geometry are not needed anymore.

In the third series of experiments we compare the kinematical splitting method for both, the Newtonian (Tab. 6) and the non-Newtonian Carreau (Tab. 5) fluid. For the Newtonian fluid we observe again higher order convergence rate in velocity. Considering the non-Newtonian rheology the convergence rate in pressure is of the second order. It is typically better than in the Newtonian case. Since the convergence of η depends on the convergence rates of $\nabla\boldsymbol{u}$ and p, we see in the case of non-Newtonian rheology improvement of the convergence order for the wall displacement, too.

Table 6: Convergence rates in space for Marchuk-Yanenko splitting, Newtonian viscosity.

# of refin.	$Err\,(\boldsymbol{u})$	EOC	$Err(\nabla\boldsymbol{u})$	EOC	$Err\,(\eta)$	EOC	$Err\,(p)$	EOC
	L^2-norm							
2/1	1.0566		1.2723		1.56e-4		3.0076	
3/2	0.2780	1.93	0.2171	2.55	1.94e-4	-0.32	0.7081	2.09
4/3	0.0872	1.67	0.0483	2.17	1.12e-4	0.79	0.0313	1.18

Now we compare the convergence results in space for four possible schemes of the kinematical splitting method, i.e. explicit Marchuk-Yanenko splitting (Tab. 7), implicit Marchuk-Yanenko splitting (Tab. 8), explicit Strang splitting (Tab. 9) and implicit Strang splitting (Tab. 10). As it is expected there is no significant improvement in the convergence rate in space due to the Strang splitting, however the implicit scheme improves the convergence rate.

The last series of experiments focuses on the evaluation of the EOC in time, that is given as follows

$$EOC(\boldsymbol{u}) = \log_2 \frac{\left(\sum_{j=1}^{N} ||\boldsymbol{u}^j_{h,\Delta t} - \boldsymbol{u}^j_{h,\Delta t/2}||^p_{L^p}/|\Omega^j_{h,\Delta t}|^p\right)^{1/p}}{\left(1/2\sum_{j=1}^{2N} ||\boldsymbol{u}^j_{h,\Delta t/2} - \boldsymbol{u}^j_{h,\Delta t/4}||^p_{L^p}/|\Omega^j_{h,\Delta t/2}|^p\right)^{1/p}}. \tag{60}$$

Here $\boldsymbol{u}^j_{h,\Delta t}$ is the velocity at the time instance $j\Delta t$. For the EOC in time, going from one

Table 7: Convergence rates in space; explicit Marchuk-Yanenko splitting, the Carreau viscosity.

# of refin	$Err\ (\boldsymbol{u})$	EOC	$Err(\nabla \boldsymbol{u})$	EOC	$Err\ (\eta)$	EOC	$Err\ (p)$	EOC
	L^p-norm				L^2-norm			
2/1	0.8667		0.9292		1.01 e-4		3.0097	
3/2	0.2338	1.89	0.1283	2.86	0.66 e-5	0.61	0.6451	2.22
4/3	0.1032	1.18	0.0437	1.55	0.25 e-5	1.37	0.1791	1.85

Table 8: Convergence rates in space; implicit Marchuk-Yanenko splitting, the Carreau viscosity.

# of refin	$Err\ (\boldsymbol{u})$	EOC	$Err(\nabla \boldsymbol{u})$	EOC	$Err\ (\eta)$	EOC	$Err\ (p)$	EOC
	L^p-norm				L^2-norm			
2/1	1.0866		0.9470		1.04e-4		3.4332	
3/2	0.3300	1.72	0.1626	2.54	4.26e-5	1.29	0.8190	2.07
4/3	0.1034	1.67	0.0442	1.88	2.51e-5	0.76	0.1960	2.06

Table 9: Convergence rates in space; explicit Strang splitting, the Carreau viscosity.

# of refin	$Err\ (\boldsymbol{u})$	EOC	$Err(\nabla \boldsymbol{u})$	EOC	$Err\ (\eta)$	EOC	$Err\ (p)$	EOC
	L^p-norm				L^2-norm			
2/1	0.8015		0.8274		9.14e-4		3.0562	
3/2	0.2144	1.90	0.1170	2.82	9.77e-5	3.23	0.5403	2.50
4/3	0.1000	1.10	0.0447	1.39	8.34e-5	0.22	0.1580	1.77

Table 10: Convergence rates in space; implicit Strang splitting, the Carreau viscosity.

# of refin	$Err\ (\boldsymbol{u})$	EOC	$Err(\nabla \boldsymbol{u})$	EOC	$Err\ (\eta)$	EOC	$Err\ (p)$	EOC
	L^p-norm				L^2-norm			
2/1	0.8646		0.9260		1.23e-4		3.0057	
3/2	0.2332	1.89	0.1280	2.86	6.11e-5	1.01	0.6420	2.23
4/3	0.1032	1.18	0.0444	1.53	2.77e-5	1.14	0.1933	1.73

time refinement to the other, the time step is halved. The time interval was $t \in [0.2; 0.8]$ and the initial time step was taken $\Delta t = 0.025$ s. In order to evaluate the EOC in time

we compute also the normalized relative $L^p(0,T;L^p(\Omega))$ error in time. This is defined by

$$Err(\boldsymbol{u}) = \frac{1}{T}\left(\sum_{j=1}^{N}\Delta t\left(\frac{||\boldsymbol{u}^j_{h,\Delta t}-\boldsymbol{u}^j_{h,\Delta t/2}||_{L^p}}{|\Omega^j_{h,\Delta t}|}\right)^p\right)^{1/p}, \quad T=N\Delta t.$$

Similarly as before, we compare the explicit and implicit Marchuk-Yanenko kinematical splitting scheme (Tabs. 11, 12) and the explicit and implicit Strang splitting scheme (Tabs. 13, 14). For the explicit kinematical splitting scheme the EOC is around first order. The second order explicit Strang splitting improves the convergence orders in comparison to the Marchuk-Yanenko splitting. The implicit kinematical splitting schemes yield better convergence than the explicit kinematical splitting schemes. Finally, Tab. 14 shows convergence rates for the implicit Strang splitting that are significantly improved. We can conclude that the Strang splitting strategy gives better convergence results for both, the explicit and the implicit schemes.

Table 11: Convergence rates in time; explicit Marchuk-Yanenko splitting, the Carreau model.

# of refin ($\triangle t$)	$Err\ (\boldsymbol{u})$	EOC	$Err(\nabla\boldsymbol{u})$	EOC	$Err\ (\eta)$	EOC	$Err\ (p)$	EOC
	$L^p(L^p)$-norm				$L^2(L^2)$-norm			
2/1	0.0246		0.0159		0.0088		0.2905	
3/2	0.0132	0.89	0.0088	0.86	0.0060	0.56	0.1422	1.03
4/3	0.0070	0.92	0.0046	0.93	0.0041	0.53	0.0697	1.03
5/4	0.0042	0.74	0.0030	0.61	0.0016	1.40	0.0336	1.05

Table 12: Convergence rates in time; implicit Marchuk-Yanenko scheme the Carreau model.

# of refin ($\triangle t$)	$Err\ (\boldsymbol{u})$	EOC	$Err(\nabla\boldsymbol{u})$	EOC	$Err\ (\eta)$	EOC	$Err\ (p)$	EOC
	$L^p(L^p)$-norm				$L^2(L^2)$-norm			
2/1	0.1491		0.1633		0.1640		0.5616	
3/2	0.1532	-0.03	0.1600	0.03	0.2706	-0.72	0.4332	0.37
4/3	0.0705	1.12	0.0747	1.10	0.2000	0.44	0.2286	0.92
5/4	0.0218	1.69	0.0234	1.67	0.0915	1.13	0.0683	1.74

Table 13: Convergence rates in time; explicit Strang splitting, the Carreau model.

# of refin ($\triangle t$)	$Err\ (\boldsymbol{u})$	EOC	$Err(\nabla \boldsymbol{u})$	EOC	$Err\ (\eta)$	EOC	$Err\ (p)$	EOC
	$L^p(L^p)$-norm				$L^2(L^2)$-norm			
2/1	0.0564		0.0252		0.0583		0.3363	
3/2	0.0195	1.53	0.0081	1.65	0.0234	1.32	0.1539	1.13
4/3	0.0077	1.34	0.0024	1.75	0.0089	1.40	0.0712	1.11
5/4	0.0044	0.83	0.0013	0.90	0.0054	0.72	0.0315	1.18

Table 14: Convergence rates in time; implicit Strang splitting, the Carreau model.

# of refin ($\triangle t$)	$Err\ (\boldsymbol{u})$	EOC	$Err(\nabla \boldsymbol{u})$	EOC	$Err\ (\eta)$	EOC	$Err\ (p)$	EOC
	$L^p(L^p)$-norm				$L^2(L^2)$-norm			
2/1	0.1826		0.1936		0.2211		0.5969	
3/2	0.0578	1.66	0.0609	1.67	0.1140	0.96	0.2411	1.31
4/3	0.0241	1.26	0.0243	1.32	0.0441	1.37	0.0896	1.43
5/4	0.0088	1.44	0.0078	1.64	0.0173	1.35	0.0297	1.60

6 Concluding remarks

In this overview paper we have summarized our recent results on mathematical modelling and numerical simulation of fluid-structure interaction of a shear-dependent non-Newtonian fluid and a viscoelastic membrane. We have presented mathematical models for both the shear-dependent fluids and the generalized string equation. Further, we have derived two fluid-structure interaction methods, the global iterative method belonging to the class of strongly coupled schemes, and the kinematical splitting which is a weakly coupled method. The global iterative method has been also used in order to prove existence of a weak solution to fully coupled interactions between the shear-dependent fluids and the viscoelastic structure. As far as we know the result presented in [25] is the first contribution to the well-posedness of fluid-structure interaction for non-Newtonian fluids.

The kinematical splitting yields a numerical scheme that is more efficient than the global iterative method while having typically smaller global errors. We have analysed stability of the semi-discrete kinematical splitting method and shown that depending on the choice of discretization for the ALE convective term we may obtain a semi-discrete scheme that does or does not depend on a time step. Indeed, using the implicit Euler time discretization we obtain the stability condition for time step depending on a mesh velocity. If the midpoint rule is used in order to discretize the ALE convective term the semi-discrete kinematical splitting is unconditionally stable, cf. also [28].

An application which is of particular interest is blood flow in elastic vessels. We have simulated blood flow in a stenotic vessel and a carotid bifurcation and analyzed some hemodynamical control quantities. We have modeled blood as a shear-thinning non-Newtonian fluid and chosen two well-known models, the Carreau model and the Yeleswarapu model. Comparisons with the Newtonian model are presented as well.

Further, we have investigated the wall deformation and the hemodynamical wall parameters, the wall shear stress WSS and the oscillatory shear index OSI, for a straight and stenotic vessel as well as for a carotid bifurcation. Numerical simulations demonstrate a significant influence of the non-Newtonian rheology for hemodynamical wall parameters. According to some authors [31] negative values of WSS indicates occurance of recirculation zones and reversal flows around stenosis, which seems to be better predicted by the non-Newtonian models. Further, the domain geometry has also a considerable influence on the wall deformation as well as on the WSS and OSI. The maximum values of OSI are larger for the Newtonian fluid. Such high OSI values at the end of stenotic occlusion indicate a large oscillatory nature of the wall shear stress and could yield further to additional stenotic plug.

Comparisons of WSS and OSI for a solid and compliant vessel showed significantly higher oscillations of the wall shear stress for fixed solid vessels. This leads to the conclusion that the fluid-structure interaction aspect is important for hemodynamical modelling and should be involved in reliable computational models.

It would be interesting to extend mathematical models and consider the generalized Oldroyd-B model that includes viscoelastic properties of blood as well. More realistic models for vessel walls, see, e.g., [6], allowing deformation in both directions would be more appropriate in order to consider more complex vessel geometries. An important point of numerical simulation is a correct outflow boundary condition, reflecting the influence of the rest of circulatory system. According to [45] this can be realized by the so-called impedance condition arising from coupling the fluid equations with some less dimensional model (1D or 0D lumped model).

Acknowledgments: This research has been supported by the European Union's 6th Framework Programme DEASE under the No. MEST-CT-2005-021122, the German Science Foundation (DFG) project ZA 613/1-1 as well as by the Nečas Centrum for Mathematical Modelling LC06052 (financed by MSMT). The third author has been partially supported by the Center for Computational Sciences in Mainz and the German Academic Exchange Service DAAD. The authors gratefully acknowledge these supports.

References

[1] Bastian P., Johannsen K., Reichenberger V.: *UG tutorial*, 2001.

[2] Bodnár T., Sequeira A.: Numerical study of the significance of the non-Newtonian nature of blood in steady flow through a stenosed vessel, In: Rannacher R. et.al. (Eds.), *Advances in Mathematical Fluid Mechanics*, 83–104, Springer Verlag, 2010.

[3] Broser Ph. J.: *Simulation von Strömungen in Blutgefässen*, Master Thesis, Ruprechts-Karl University, Heidelberg, 2001.

[4] Bucur D., Fereisl E., Nečasová Š.: Influence of wall roughness on the slip behavior of viscous fluids, *Proc. R. Soc. Edinb., Sect. A, Math.* 138(5) (2008), 957-973.

[5] Bucur D., Feireisl E., Nečasová Š., Wolf J.: On the asymptotic limit of the Navier-Stokes system on domains with rough boundaries, J. of Differ. Equations 244 (2008), 2890–2908.

[6] Čanić S., Tambača J., Guidoboni G., Mikelič A., Hartley C.J., Rosenstrauch D.: Modeling viscoelastic behavior of arterial walls and their intercation with pulsatile blood flow, *SIAM J. Appl. Math.* 67(1) (2006), 164–193.

[7] Chambolle A., Desjardin B., Esteban M.J., Grandmont C.: Existence of weak solutions for unsteady fluid-plate interaction problem, *J. Math. Fluid Mech.* 7 (3) (2005), 368–404.

[8] Černý J.: Numerical modelling of non-Newtonian flows with application in hemodynamics, *Report TU Hamburg-Harburg*, 2004.

[9] Cheng A., Shkoller S.: The interaction of the 3D Navier-Stokes equations with a moving nonlinear Koiter elastic shell, *SIAM J. Math. Anal.* 42(3) (2010), 1094-1155.

[10] Cheng A., Coutand D., Shkoller S.: Navier-Stokes equations interacting with a nonlinear elastic biofluid shell, *SIAM J. Math. Anal.* 39(3) (2007), 742-800.

[11] Coutand D., Shkoller S.: Motion of an elastic solid inside an incompressible viscous fluid, *Arch. Ration. Mech. Anal.* 176(1) (2005), 25-102.

[12] Coutand D., Shkoller S.: Interaction between quasilinear elasticity and the Navier-Stokes equations, *Arch. Ration. Mech. Anal.* 179 (2006), 303-352.

[13] Filo J., Zaušková A.: 2D Navier-Stokes equations in a time dependent domain with Neumann type boundary conditions, *J. Math. Fluid Mech.* 10 (2008), 1–46.

[14] Formaggia L., Gerbeau J.F., Nobile F., Quarteroni A.: On the coupling of 3D and 1D Navier-Stokes equations for flow problems in compliant vessels, *Comput. Meth. Appl. Mech. Eng.* 191 (6-7) (2001), 561–582.

[15] Formaggia L., Nobile F.: A stability analysis for the arbitrary Lagrangian Eulerian formularion with finite elements, *East-West J. Numer. Math.* 7 (2) (1999), 103–131.

[16] Förster C., Scheven von M., Wall W.A., Ramm E.: Coupling of incompressible flows and thin-walled structures, In: Papadrakakis M. et. al. (Eds.) *Coupled Problems 2007 International Conference on Computational Methods for Coupled Problems in Science and Engineering*, 541–544, Greece, 2007.

[17] Frehse J., Málek J., Steinhauer M.: On analysis of steady flow of fluid with shear dependent viscosity based on the Lipschitz truncation method, *SIAM J. Math. Anal.* 35(5) (2003), 1064–1083.

[18] Galdi G.P., Rannacher R., Robertson A.M., Turek S.: *Hemodynamical Flows. Modeling, Analysis, Simulation.*, Oberwolfach Seminars Vol. 37, Birkhäuser Verlag, 2008.

[19] Gijsen F.J.H., van de Vosse F.N., Janssen J.D.: Influence of the non-Newtonian properties of blood flow on the flow in large arteries: steady flow in a carotid bifurcation model, *J. Biomech.* 32 (1999), 601–608.

[20] Grandmont C.: Existence of weak solutions for the unsteady interaction of a viscous fluid with an elastic plate, *SIAM J. Math. Anal.* 40(2) (2008), 716-737.

[21] Guidoboni G., Glowinski R., Cavallini N., Čanić S.: Stable-loosely coupled-type algorithm for fluid-structure interaction on blood flow, *J. Comput. Phys.* 228 (18) (2009) 6916–6937.

[22] Guidoboni G., Guidorzi M., Padula M.: Continuous dependence on initial data in fluid-structure motion, *J. Math. Fluid Mech.* (2010) published online: http://dx.doi.org/10.1007/s00021-010-0031-0.

[23] Guidorzi M., Padula M., Plotnikov P.I.: Hopf solutions to a fluid-elastic interaction model, *Math. Models Meth. Appl. Sci.* 18 (2) (2008), 215–270.

[24] Hundertmark-Zaušková A., Lukáčová-Medviďová M.: Numerical study of shear-dependent non-Newtonian fluids in compliant vessels, *Comput. Math. Appl.* 60 (2010), 572–590.

[25] Hundertmark-Zaušková A., Lukáčová-Medviďová M., Nečasová Š.: On the existence of a weak solution to the coupled fluid-structure interaction problem for the non-Newtonian shear-dependent fluid, *Preprint University of Mainz*, 2011.

[26] Lesoinne M., Farhat Ch.: Geometric conservation laws for flow problems with moving boundaries and deformable meshes and their impact on aeroelastic computations, *Comput. Meth. Appl. Mech. Eng.* 134 (1996), 71–90.

[27] Lukáčová-Medviďová M., Černý J.: Numerical modelling of non-Newtonian shear-thinning viscoelastic fluids with application in hemodynamics, In: Sequeira A. et.al. (Eds.) *Proceedings of the Second International Symposium Modelling of Physiological Flows*, Portugal, 2005.

[28] Lukáčová-Medviďová M., Rusnáková G.: Kinematical splitting algorithm for fluid-structure interaction in hemodynamics, *Preprint University of Mainz & University of Košice*, 2011.

[29] Lukáčová-Medviďová M., Zaušková A.: Numerical modelling of shear-thinning non-Newtonian flows in compliant vessels, *Int. J. Numer. Methods Fluids*, 56 (2008), 1409–1415.

[30] Malek A.M., Alper A.L., Izumo S.: Hemodynamic shear stress and its role in atherosclerosis, *J. Am. Med. Assoc.* 282 (1999), 2035–2042.

[31] Nadau L., Sequeira A.: Numerical simulations of shear dependent viscoelastic flows with a combined finite element - finite volume method, *Comput. Math. Appl.* 53 (2007), 547–568.

[32] Nägele S.: *Mehrgitterverfahren für incompressiblen Navier-Stokes Gleichungen im laminaren und turbulenten Regime unter Berücksichtigung verschiedener Stabilisierungsmethoden*, PhD Thesis, Ruprechts-Karl University, Heidelberg, 2003.

[33] Neustupa J.: Existence of weak solution to the Navier-Stokes equation in a general time-varying domain by Rothe method, *Math. Methods Appl. Sci.* 32(6) (2009), 653–683.

[34] Málek J., Nečas J., Ružička M.: On the weak solutions to a class of non-Newtonian incompressible fluids in bounded three-dimensional domans: the case $p \geq 2$, *Adv. Differ. Equat.* 6(3) (2001), 257–302.

[35] Málek J., Nečas J., Rokyta M., Ružička M.: *Weak and Measure-Valued Solutions to Evolutionary PDEs*, Chapman and Hall, London, 1996.

[36] Nobile F.: *Numerical Approximation of Fluid-Structure Interaction Problems with Application to Haemodynamics*, PhD Thesis, EPFL Lausanne, 2001.

[37] Perktold K., Rappitsch G.: Mathematical modelling of local arterial flow and vessel mechanics, In: Crolet J.-M. et.al. (Eds.) *Computational Methods for Fluid-Structure Interaction*, 230–245, Longman, Harlow, 1994.

[38] Perktold K., Resch M., Reinfried O.P.: Three-dimensional analysis of pulsative flow and wall shear stress in the carotid artery bifurcation, *J. Biomech.* 24(6) (1991), 409–420.

[39] Quarteroni A.: Mathematical and numerical simulation of the cardiovascular system, In: *Proceedings of the International Congress of Mathematicians, Vol. III*, 839–849, Higher Ed. Press, Beijing, 2002.

[40] Quarteroni A., Formaggia L.: Mathematical modelling and numerical simulation of the cardiovascular system, In: Ciarlet P.G. et. al. (Eds.) *Handbook of Numerical Analysis*, Elsevier, Amsterdam, 2002.

[41] Quarteroni A., Gianluigi R.: Optimal control and shape optimization of aorto-coronaric bypass anastomoses, M^3AS, *Math. Models Methods Appl. Sci.* 13 (12) (2003), 1801–1823.

[42] Quarteroni A., Valli A.: *Numerical Approximation of Partial Differential Equations*, Springer Verlag, 2008.

[43] Rajagopal K., Lawson J.: Regulation of hemostatic system function by biochemical and mechanical factors, Modeling of Biological Materials, In: Bellomo N. (Ed.) *Modeling and Simulation in Science, Engineering and Technology*, 179–201, Birkhäuser, Boston, 2007.

[44] Surulescu C.: On the stationary interaction of a Navier-Stokes fluid with an elastic tube wall, *Appl. Anal.* 86(2) (2007), 149–165.

[45] Taylor Ch.A., Vignon-Clementel I.E., Figueroa C.A., Jansenca K.E.: Outflow boundary conditions for three-dimensional finite element modeling of blood flow and pressure in arteries, *Comput. Meth. Appl. Mech. Eng.* 195 (2006), 3776–3796.

[46] Taylor Ch.A.., Hughes J.R., Zarins C.K.: Effect of exercise on hemodynamic conditions in the abdominal aorta, *J. Vasc. Surg.*, 29 (6) (1999), 1077–1089.

[47] da Veiga B. H.: On the existence of strong solution to a coupled fluid-structure evolution problem, *J. Math. Fluid Mech.* 6 (1) (2001), 21–52.

[48] Yeleswarapu K.K.: *Evaluation of Continuum Models for Chatacterizing the Constitutive Behavior of Blood*, PhD Thesis, University of Pittsburg, 1996.

[49] Yeleswarapu K.K., Kameneva M.V., Rajagopal K.R., Antaki J.F.: The flow of blood in tubes: theory and experiments, *Mech. Res.Commun.* 25 (3) (1998), 257–262.

[50] Wolf J.: Existence of weak solution to the equations of non stationary motion of non-Newtonian fluids with shear rate dependent viscosity, *J. Math. Fluid Mech.* 9 (2007) 104–138.

[51] Zaušková A.: *2D Navier-Stokes Equations In a Time Dependent Domain*, PhD Thesis, Comenius University, Bratislava, 2007.